

SPECTROSCOPY OF LOW SURFACE BRIGHTNESS GALAXIES WITH THE HOBBY-EBERLY TELESCOPE

MARCEL BERGMANN

Astronomy Department, University of Texas, Austin, TX 78712
marcel@astro.as.utexas.edu

AND

INGER JØRGENSEN

Gemini Observatory, Hilo, HI 96720
ijorgensen@gemini.edu

AND

GARY J. HILL

McDonald Observatory, University of Texas, Austin, TX 78712
hill@astro.as.utexas.edu

Accepted for publication in the Astronomical Journal

ABSTRACT

We have obtained low resolution spectra of nineteen red and blue low surface brightness galaxies, using the Marcario Low Resolution Spectrograph on the 9.2m Hobby-Eberly Telescope. These galaxies form a very heterogeneous class, whose spectra qualitatively resemble those of high surface brightness galaxies covering the full range of spectra seen in galaxies of Hubble types from E to Irr. We use a combination of emission line (EW(H α), [N II] λ 6584/H α) and absorption line (Mgb, H β , <Fe>) based diagnostics to investigate the star-formation and chemical enrichment histories of these galaxies. These are diverse, with some galaxies having low metallicity and very young mean stellar ages, and other galaxies showing old, super-solar metallicity stellar populations. In contrast with some previous studies which found a strong trend of decreasing metallicity with decreasing central surface brightness, we find a population of galaxies with low surface brightness and near-solar metallicity. Correlations between several of the gas phase and stellar population age and metallicity indicators are used to place constraints on plausible evolutionary scenarios for LSB galaxies. The redshift range spanned by these galaxies is broad, with radial velocities from 3400 km/s to more than 65000 km/s. A subset of the sample galaxies have published H I redshifts and gas masses based on observations with the Arecibo 305m single-dish radio telescope, which place these galaxies far off of the mean Tully-Fisher relation. Our new optical redshifts do not agree with the published H I redshifts for these galaxies. Most of the discrepancies can be explained by beam confusion in the Arecibo observations, causing erroneous H I detections for some of the galaxies.

Subject headings: galaxies: abundances — galaxies: distances and redshifts — galaxies: stellar content — galaxies: fundamental parameters — galaxies: formation and evolution

1. INTRODUCTION

The class of low surface brightness (LSB) galaxies is a diverse one. LSB galaxies exhibit a range of absolute magnitudes, colors, and morphologies comparable to those of high surface brightness (HSB) galaxies. The defining characteristic of LSB galaxies is, of course, their faint central surface brightness, variously defined as being at least one magnitude fainter than the canonical Freeman (1970) value of 21.65 B mag/ \square'' , or fainter than 23 B mag/ \square'' ; the precise limit varies from investigator to investigator. However, whether the low surface brightness results from a common evolutionary history for these galaxies remains unknown.

Studies of LSB galaxies fall into two broad classes. The first class comprises the surveys to find LSB galaxies, and attempts to quantify what fraction of the total galaxy number density, luminosity density, and mass density are made up by them. The second class comprises studies of the internal structure of LSB galaxies, including investigations into their gas content, star formation history, and evolutionary processes.

The large area surveys which were initially mined for LSB galaxies were photographic surveys, including the Uppsala Galaxy Catalog (UGC; Nilson 1973), the POSS-2 survey (Schombert & Bothun 1988; Schombert et al. 1992), and the APM survey (Impey et al. 1996). In the past decade, large area CCD surveys have also found a significant population of LSB galaxies. Notable among these are the drift scan survey of Dalcanton et al. (1997), who use well quantified automated detection methods, and the multicolor survey of O'Neil, Bothun, & Cornell (1997, hereafter OBC97) and O'Neil et al. (1997b, hereafter OBSCI97), which turned up a previously unseen population of red LSB galaxies.

These surveys proved the existence of LSB galaxies as more than the occasional oddity. Dalcanton et al. (1997) make a conservative estimate of the number density of LSB galaxies of $N = 0.01^{+0.006}_{-0.005}$ galaxies $h_{50}^3 \text{Mpc}^{-3}$, equal to the number density of HSB galaxies. However, the Dalcanton et al. survey suffers from small number statistics, with only 7 LSBs detected. McGaugh, Bothun, & Schombert (1995) have a larger sample, and come to a similar conclusion about the LSB galaxy number density. More recently,

de Jong & Lacey (2000) have used a photographic survey of $\simeq 1000$ Sb-Sdm galaxies to calculate the bivariate luminosity and number density of galaxies as a function of both surface brightness and scale length. They find that while the luminosity density is dominated by HSB galaxies (peaked at $\mu_B(0) \simeq 21.0$ mag/ \square''), the number density of galaxies has an essentially flat distribution at all surface brightnesses fainter than $\mu_B(0) \simeq 21.0$ mag/ \square'' , and therefore LSB galaxies make up a significant fraction of the total number of galaxies (See also the surveys of O’Neil & Bothun (2000) and Cross & Driver (2002)).

The best studied LSB disk galaxies are those in the thesis sample of de Blok (1997), originally selected from the photographic survey catalogs of Schombert et al. (1992) and the UGC catalog. Observations of these ~ 20 galaxies include multicolor optical surface photometry (de Blok, van der Hulst, & Bothun 1995), VLA mapping of the H I distribution and kinematics (de Blok, McGaugh, & van der Hulst 1996; de Blok & McGaugh 1997), and spectroscopy of the H II regions (de Blok & van der Hulst 1998). The general picture obtained from these observations is that LSB galaxies are metal poor and gas rich, with a range of sizes (scale lengths) comparable to HSB galaxies, but with much lower surface densities. However, note that de Blok’s selection criteria included an existing H I detection. The kinematics, and therefore the gravitational potentials, are dominated by dark matter at all radii (de Blok & McGaugh 1997; McGaugh, Rubin, & de Blok 2001), and the low global star formation rates (SFR) are the combined result of both the low surface density, and the low metallicity (Gerritsen & de Blok 1999).

Sprayberry, Impey, Bothun, & Irwin (1995) obtained photometry, low-resolution optical spectroscopy, and HI spectroscopy for a sample of 8 giant LSB galaxies. Their optical spectroscopic data pertain primarily to the bulges of these galaxies, and they find no difference between the bulges of large LSB and HSB galaxies.

The wide field CCD survey of OBC97 found a large number of LSB galaxies, covering a wider range of colors than those found by previous photographic surveys. In particular, red LSB galaxies with $(B-V) > 0.9$, colors consistent with purely old stellar populations, were catalogued for the first time. The follow-up single dish H I observations using the Arecibo 305m single-dish radio telescope (O’Neil, Bothun, & Schombert 2000a) suggested that many of these red LSBs (and some of the blue LSBs) were quite peculiar indeed, having gas mass-to-light ratios (M/L) in excess of 8, with a few higher than 30. Further, the rotational line widths were far larger than would be expected from their luminosities given the standard Tully-Fisher (1977) relation for spiral galaxies.

Larger scatter in the Tully-Fisher relation among LSB galaxies was also measured by Burkholder, Impey, & Sprayberry (2001). Their survey of over 250 HSB and LSB galaxies selected from the APM survey (Impey et al. 1996) included photometry, HI spectroscopy, and low resolution optical spectroscopy (Impey, Burkholder, & Sprayberry 2001; Burkholder, Impey, & Sprayberry 2001). They used emission line ratios to measure the metallicity for 49 HSB and 17 LSB galaxies (where they define $\mu_B = 22$ mag/ \square'' as the dividing line) and found there to be a roughly 50% overlap in the metallicity range of the two groups.

Bell et al. (2000) combined optical and near-infrared surface photometry to study the stellar populations in subsets of both the de Blok sample and the red galaxies from the OBSCI97 survey. Broadband optical studies of stellar populations suffer from a degeneracy in color space between age and metallicity; red colors could indicate either older stars or more metal-rich stars, while bluer colors indicate either younger stars or metal-poor stars. The inclusion of near-infrared colors partially breaks this degeneracy, essentially giving a handle on the fractional light contribution from old stars which dominate the light in the near-infrared, and younger stars which will dominate at bluer wavelengths. Bell et al. found that the bluer galaxies from the de Blok sample were younger than similar HSB late-type galaxies. Further, the five red LSB galaxies in their study were a mixture of two types: genuinely red galaxies with old stellar populations, but central surface brightnesses on the bright end of the LSB range (~ 22.5 mag/ \square'' in B), and a group of objects with lower surface brightness whose true colors, after correcting for galactic extinction, were in fact as blue as the de Blok sample galaxies and had similar stellar mean ages. Interestingly, the three red galaxies with old stellar populations were not detected in the O’Neil et al. (2000a) H I survey, while the two galaxies with blue extinction corrected colors were detected. However, none of the red galaxies with extreme M_{HI}/L ratios were studied by Bell et al.

We have obtained spectra for a sample of 19 red and blue LSB galaxies chosen from the catalog of OBC97, with the intent of studying the star formation histories of these galaxies. Using a combination of emission and absorption line measures, we compare the chemical enrichment of the stars and gas, and we use the stellar population models of Vazdekis (1999, 2000¹, hereafter V1999 and V2000, respectively) to interpret these data quantitatively. In particular, we attempt to determine whether a single LSB galaxy formation model can be reconciled with the various observational attributes of these galaxies.

This paper is organized as follows. In Section 2 we present the sample, the spectroscopic and photometric observations, and the data reduction. Sections 3 through 8 presents the LSB spectra, analysis of the emission line and absorption index strengths, and comparison to HSB galaxies. We discuss these results in the context of LSB formation models in Section 9. Finally, we summarize our conclusions in Section 10.

2. OBSERVATIONS & DATA REDUCTION

2.1. Sample selection for the spectroscopic observations

This project began during the early science operations of the Hobby-Eberly Telescope (HET; Ramsey et al. 1998) in 1999 November and observations continued through 2001 January. For the first set of spectroscopic observations, during winter 1999-2000, we chose a group of LSB galaxies from the sample of OBC97 which covered a range of color ($0.3 < B-V < 1.35$) and central surface brightness ($22.0 < \mu_B(0) < 24.0$). Twelve galaxies were observed during the first observing period. A new sample of six galaxies was chosen for observation during winter 2000-2001. These objects were selected from the H I follow-up survey of O’Neil et al. (2000a), and stand out due to their extremely

¹ http://www.iac.es/galeria/vazdekis/MODELS_2000/out_li_BI

TABLE 1
LITERATURE DATA FOR GALAXIES IN SPECTROSCOPIC SAMPLE^a

galaxy	RA	Dec	cz (HI)	r_e	B(5'') ^b	I _c (5'') ^b	B _{tot} ^b	I _{ctot} ^b	$\mu_B(0)_{cor}$ ^b	i ^c	E(B-V)
(1)	(J2000) (2)	(J2000) (3)	(km s ⁻¹) (4)	('') (5)	(mag) (6)	(mag) (7)	(mag) (8)	(mag) (9)	(mag/□'') (10)	(deg) (11)	(12)
[OBC97]P1-3	23:21:18	08:14:28	3746	7.1	18.28	16.70	17.15	15.81	22.2	45	0.071
[OBC97]P6-1	23:23:33	08:37:25	10882	18.9	19.55	16.79	17.23	15.04	24.2	66	0.061
[OBC97]P9-4	23:18:40	07:30:44	4205	10.9	20.84	18.23	18.86	16.29	25.0	67	0.144
[OBC97]C1-2	08:19:55	20:51:43	8531	5.2	18.99	16.91	18.10	15.84	22.5	21	0.049
[OBC97]C1-4	08:19:24	21:00:12	...	12.6	18.09	15.80	16.55	14.48	22.3	63	0.050
[OBC97]C3-2	08:22:36	20:59:46	...	6.0 ^d	18.17	16.06±0.06	16.34	14.14	22.8	47	0.038
[OBC97]C4-1	08:24:33	21:27:04	7905	11.0 ^d	18.97	...	17.83	...	23.6	39	0.044
[OBC97]C4-5	08:25:48	21:52:45	...	5.6	18.96	...	18.23	...	23.0	57	0.046
[OBC97]C5-3	08:27:44	22:28:52	12942	8.6	20.12	18.31±0.1	18.88	16.37	24.0	20	0.041
[OBC97]C5-5	08:27:12	22:53:39	5524	23.0	19.90±0.2	18.60±0.2	18.08±0.2	16.19±0.2	24.3	45	0.038
[OBC97]C6-1	08:27:31	21:30:03	4322	6.5	18.57	16.22±0.06	17.53	15.27	22.5	44	0.041
[OBC97]C8-3	08:17:17	21:39:12	3570	4.8	19.22	...	17.69	...	24.3	72	0.039
[OBC97]N3-1	12:32:59	07:29:26	...	8.6	19.05	...	18.02	...	23.5	64	0.023
[OBC97]N9-1	10:20:18	27:45:10	...	7.6	18.41	19.18±1	17.29	17.60±1	22.3	41	0.036
[OBC97]N9-2	10:20:22	28:07:56	7746	6.4	19.80	20.59±0.06	18.89	17.49	24.0	47	0.037
[OBC97]N10-2	11:58:42	20:34:43	...	10.8	18.03	16.22±0.06	16.57	14.85	22.8	52	0.023
[OBC97]N10-4	11:58:52	20:58:28	7478	9.6	19.94	...	18.90	...	24.2	31	0.027
[OBC97]U1-4	11:38:25	17:05:14	3450	32.5	19.00	17.26±0.06	13.08	12.21	23.3	55	0.025
[OBC97]U1-8	11:39:23	16:50:31	...	10.3	19.30	16.55±0.06	18.15	15.65	24.1	70	0.025

^aColumns (1)-(3) give the names and positions from O'Neil et al. (2000a), and the redshifts of their HI detections are listed in column (4). The exponential scale lengths measured by OBC97 have been converted to half light radii using the formula $r_e = 1.68\alpha$ (Sparks 1988), and these are listed in column (5). Columns (6)-(7) list the B-band and I-band magnitudes inside apertures of radius 5'', and the corresponding total magnitudes are given in columns (8)-(9) (OBC97, OBSCI97). The inclination corrected B band central surface brightnesses are given in column (10), and the inclinations are in column (11), both from OBC97. Column (12) lists the galactic extinction derived from the Schlegel et al. (1998) dust maps.

^bUnless otherwise noted, the typical intrinsic uncertainty on the photometry is reported to be ± 0.05 mag for the aperture magnitudes, and ± 0.1 mag for the total magnitudes and $\mu_B(0)_{cor}$. The uncertainty in the photometric zeropoints are 0.03 mag in the B-band, and 0.04 mag in the I-band (OBC97, OBSCI97).

^cThe intrinsic uncertainty on the inclination angle is $\pm 5^\circ$ (OBC97).

^dNot measured by OBC97. We use this value for spectral extraction to optimize the signal-to-noise ratio. (see Sect. 2.3.3).

high M_{HI}/L_B , and that they lie more than 5σ from the I-band Tully-Fisher relation (Tully & Fisher 1977; Pierce & Tully 1988). Additionally, one galaxy ([OBC97]P06-1²) was chosen because it is the first LSB (albeit a giant LSB) galaxy for which CO has been detected (O'Neil, Hofner, & Schinnerer 2000b; see also Matthews & Gao 2001). These seven galaxies fall into the same range of color and central surface brightness as the original sample. We obtained spectra for a total of 19 galaxies. Table 1 lists the galaxies in our spectroscopic sample, along with positions and relevant data from the literature.

2.2. Photometry

2.2.1. Observations & Basic Reductions

We obtained new photometry for a subset of the LSB galaxies in the spectroscopic sample, using the Prime Focus Camera (PFC; Claver 1995) on the McDonald Observatory 0.8m telescope in November and December of 1999. The PFC is a wide-field imager, with a $45' \times 45'$ field of view. The wide-field images include eleven of the nineteen galaxies in the spectroscopic sample, as well as sixteen galaxies from the OBC97 catalog not included in our spectroscopic observations. The instrumental configuration is given in Table 2. Images were taken through the B, R_c, and I_c filters, centered on the OBC97 survey fields C1, C3, C4, C5, N9, and U1. Multiple images were taken in each band to aid in cosmic ray rejection. Ad-

² The official (IAU) names for the LSB galaxies in this work originated in OBC97, and are listed in full in Table 1. For convenience, however, we will use abbreviated galaxy names without [OBC97] for the remainder of this paper.

ditionally, we took images of 10 fields containing a total of 217 standard stars included in Landolt (1992) to facilitate photometric calibration of the data. For each field observed, Table 3 lists the position of the field center, the total integration time and number of exposures through each filter, and the image quality of the coadded data, described in terms of the FWHM and ellipticity of the PSF as determined from gaussian fits to radial profiles of more than 100 stars per image.

Data reduction was done within the IRAF³ environment. The images were overscan and bias subtracted, then a shutter correction was applied. Next, the images were divided by a normalized dome flatfield, as well as a normalized illumination correction. The illumination correction is a highly clipped average of all science frames observed at low airmass, in the absence of clouds or moonlight, and corrects large scale gradients not reproduced by the dome flatfield image. After this step, the science images were individually examined for residual real gradients caused by scattered moonlight, clouds, or sky illumination (see Chromey & Hasselbacher 1996). Any residual gradients larger than 1% across the full image were fit using `imsurfit` and subtracted off, with the mean sky level then added back in as a constant to maintain counting statistics.

Prior to coaddition, a badpixel mask was generated for each image by taking the standard mask file for the CCD,

³ IRAF is distributed by the National Optical Astronomy Observatories, which are operated by the Association of Universities for Research in Astronomy, Inc., under cooperative agreement with the National Science Foundation.

TABLE 2
INSTRUMENTATION

	Spectroscopy	Photometry
Telescope	Hobby-Eberly Telescope (9.2m)	McDonald Observatory 0.8m
Instrument	Low Resolution Spectrograph	Prime Focus Camera
Dates	10/99-2/01	11/99-12/99
CCD	Ford Aerospace 3072 × 1024 (binned 2 × 2)	Loral-Fairchild 2048 × 2048
Gain	1.82e ⁻ /ADU	1.6 e ⁻ /ADU
RON	7.0 e ⁻	5.87e ⁻
Pixel size spatial	0.465''	1.354''
Wavelength Range	4300Å - 7240 Å	B, R _c , I _c
Slit Width × Length	2'' × 4'	...
Grism	600 l/mm	...
Dispersion	2Å/pix	...
Resolution(σ)	3.3Å (190 km s ⁻¹ @ 5200Å)	...

TABLE 3
PFC PHOTOMETRY OBSERVATIONS

Field ^a	Filter	Exposure Time ^b	N _{obs} ^c	FWHM _{PSF} ^d	ε _{PSF} ^e	N _{PSF} ^f
C1	B	300	1	2.8	0.12	176
(08:19:52.6 +21:00:17)	R _c	180	1	2.7	0.13	111
	I _c	120	1	2.4	0.12	101
C3	B	1500	3	3.0	0.08	229
(08:22:46.6 +21:03:34)	R _c	780	3	2.7	0.06	176
	I _c	600	3	3.0	0.04	127
C4	B	2100	4	2.8	0.05	508
(08:26:01.3 +21:57:06)	R _c	1380	5	2.8	0.04	201
	I _c	600	3	3.0	0.06	109
C5	B	2100	4	3.1	0.10	180
(08:26:54.1 +22:35:23)	R _c	1080	4	3.0	0.04	126
	I _c	600	3	3.1	0.07	145
N9	B	2100	4	3.2	0.07	264
(10:20:29.3 +27:55:29)	R _c	780	3	2.8	0.07	141
	I _c	600	3	3.0	0.05	118
U1	B	1200	2	3.8	0.04	147
(11:39:29.1 +17:04:21)	R _c	1200	4	3.2	0.03	101
	I _c	720	3	3.5	0.06	145

^aFirst row of each entry is the field name from OBC97. Second row lists the coordinates (J2000) of the field center.

^bTotal exposure time for all observations, in seconds.

^cNumber of individual exposures.

^dMean full-width at half-maximum of a gaussian fit to the point-spread-function (PSF), measured in arcsec.

^eMean measured ellipticity of the PSF.

^fNumber of stars used in determination of FWHM and ε.

and manually adding all the pixels affected by satellite trails or by ghost images caused by reflections within the PFC optics. The coaddition process was done using the task `imcoadd` (Jørgensen, in prep.) in the Gemini IRAF package. This task determines spatial offsets between all the input images, shifts them accordingly, generates cosmic ray masks, and averages all the good pixel values to produce a coadded output image. The photometric zeropoint offsets between all the input images and the output image were determined. As long as at least one input image was taken during photometric conditions, the coadded output can then be easily calibrated onto a standard system. Finally, we used the HST guide star catalog reference frame to establish the world coordinate system (WCS) for the coadded images.

2.2.2. Object Extraction & Standard Photometry

Object extraction was done using SExtractor (version 2.1.6; Bertin & Arnouts 1996), and the output catalogs were matched using the WCS positions to produce a single table with photometry in all three bands (B, R_c , I_c) for each object.

To calibrate the photometry onto a standard system, we used observations of the Landolt (1992) selected area fields SA92, SA95, SA98, SA101, SA104, and SA113, as well as the fields near the standards PG0918+029, PG0231+051, PG1633+091, and PG0233+051. Observations were made each photometric night, interspersing science and standard fields. In total, we have 380 stellar observations in each of the three bands, covering 217 different stars. The standard fields were observed over a range of airmasses spanning from 1 to 3, to better constrain the extinction coefficients. In contrast, the science fields were all observed in the airmass range 1 to 1.25. Average extinction coefficients covering all three photometric nights were used in the standard calibration. The rms scatter of the final standard calibration of the photometric zeropoints was 0.06 mag (B), 0.05 mag (R_c), and 0.05 mag (I_c).

There were no observations of field U1 taken during photometric conditions. To calibrate this field, we used the ~ 1000 stars in our observation in common with the USNO-A2.0 catalog (Monet et al. 1998). We derived relations between the SExtractor “best” magnitudes and the USNO magnitudes for both the U1 and N9 fields, and used the zeropoint offset between these two relations to calibrate the photometry for the U1 field to the standard system. The USNO magnitudes do not have to be on a standard system to make this technique work, merely be internally consistent. The extra uncertainty contributed by this calibration is 0.02 mag, smaller than our zeropoint uncertainty as derived using SExtractor.

We applied galactic extinction corrections to our photometry based on reddening values derived from the Schlegel et al. (1998) dust maps, and the coefficients derived by them for extinction in each band versus color excess (e.g. $A_B/E(B-V) = 4.315$, $A_V/E(B-V) = 3.315$, $A_{R_c}/E(B-V) = 2.673$, $A_{I_c}/E(B-V) = 1.940$). Table 4 lists the extinction corrected magnitudes for the 27 galaxies in the OBC97 sample that are included in our observations with the PFC. Also listed are the $E(B-V)$ values used to determine the extinction correction in each band.

2.2.3. Comparison to literature data

We have compared our photometry with the measurements of OBC97 and OBSCI97 (which were also obtained with the PFC). Figure 1 shows the comparison.

Figures 1a and 1c show the comparison of the aperture magnitudes in the B-band and I-band, respectively. In the B-band, we find an offset of -0.52 ± 0.04 mag with an rms scatter of 0.19 mag (excluding the two most deviant measurements, N9-2 and C4-2). Offsets are our magnitudes minus OBC97 magnitudes. In the I-band, we find an offset of -0.31 ± 0.08 mag with an rms scatter of 0.34 mag (excluding N9-1 and N9-2). The offsets and the large scatter may be due to the sensitivity of the small apertures used ($5''$) to changes in seeing or image quality. In the interim between when OBC97 obtained their data and the time when we made our observations, the PFC optics were anti-reflection coated and re-aligned, which improved the delivered image quality. In our coadded images, the stellar PSF has a typical FWHM of 2.2 pixels ($2.9''$), with an ellipticity of 0.07. O’Neil has provided some of her images to the NED¹ database, and the typical image quality we measure for these small images is ~ 3 pixels fwhm ($4''$). Poorer image quality will scatter more of the light outside the small $5''$ aperture, resulting in fainter aperture magnitude measurements, consistent with the offsets we see.

OBC97 derive total magnitudes from exponential and King profile fits to the galaxy surface brightness profiles. We compare these to the SExtractor “best” magnitudes, which are also a measure of the total magnitude (though systematically too faint by 6%, see Bertin & Arnouts (1996) for details) in Figures 1b and 1d. The agreement in the B-band is good, except for two outliers, N9-2 and U1-4. Examination of the surface brightness profiles in OBC97 for these two objects shows the profiles to be more complex than could be well fit by a single exponential. Excluding these two points, the offset between the two datasets is -0.11 ± 0.04 mag with an rms scatter of 0.21 mag. In the I-band, the offset is 0.23 ± 0.08 mag with an rms scatter of 0.33 mag.

We have not measured central surface brightness, $\mu(0)$, from our photometry, so we cannot compare to the values in OBC97. However, since they derive total magnitudes based on $\mu(0)$ and the exponential scale length (α , derived over an area with radius typically larger than $12''$), we expect offsets in $\mu(0)$ to be comparable to offsets in the total magnitudes, which are small in the B-band.

Figures 1e 1f show the comparisons of the ($B-I_c$) aperture and total colors, respectively, with the results from OBSCI97. For both the aperture and total colors, we derive a zeropoint offset of -0.24 ± 0.07 mag with an rms scatter of 0.30 mag, when we exclude the two most deviant points (N9-1 and N9-2 for the aperture colors, N9-1 and C5-3 for the total colors). For N9-1 the uncertainty on ($B-I_c$) from OBSCI97 is 1 mag. The typical intrinsic uncertainty for our ($B-I_c$) color measurements is 0.05 mag, derived from the SExtractor uncertainties on the individual band magnitudes, added in quadrature. In the following analysis we use our new photometry when available. For the remaining galaxies with spectroscopic observations we use photometry from OBC97. We calibrate the colors from OBSCI97 to be consistent with our data by applying an offset of -0.24 mag, and adopt an uncertainty in this

¹ <http://ned.ipac.caltech.edu>

TABLE 4
NEW PHOTOMETRY FROM PFC OBSERVATIONS^a

Name	B(5'')	R _c (5'')	I _c (5'')	B _{tot}	R _{c,tot}	I _{c,tot}	E(B-V)
C1-1	17.95±0.03	16.31±0.01	15.70±0.01	17.05±0.05	15.59±0.02	15.12±0.02	0.051
C1-2	18.66±0.06	17.26±0.03	16.80±0.04	17.79±0.08	16.57±0.04	15.97±0.06	0.049
C1-4	17.45±0.02	16.01±0.01	15.44±0.01	16.35±0.03	14.89±0.01	14.32±0.02	0.050
C1-6	17.53±0.02	16.48±0.01	15.99±0.02	16.57±0.03	15.49±0.02	15.07±0.03	0.051
C3-1	18.26±0.01	16.63±0.01	16.02±0.01	17.21±0.02	15.84±0.01	15.30±0.01	0.034
C3-2	17.60±0.01	16.24±0.00	15.65±0.00	16.38±0.01	15.02±0.01	14.39±0.01	0.038
C3-6	17.81±0.01	16.60±0.01	16.06±0.01	16.62±0.01	15.42±0.01	14.88±0.01	0.049
C4-1	18.58±0.03	18.00±0.03	17.67±0.03	17.71±0.05	17.08±0.04	16.61±0.05	0.044
C4-2	19.05±0.05	18.32±0.04	17.84±0.04	17.50±0.06	16.62±0.04	16.09±0.04	0.047
C4-3	18.46±0.03	17.67±0.02	17.22±0.02	17.33±0.04	16.55±0.03	16.07±0.03	0.048
C4-5	18.62±0.03	17.50±0.01	16.99±0.04	18.05±0.03	16.85±0.02	16.36±0.06	0.046
C4-6	17.65±0.01	16.23±0.00	15.97±0.02	17.47±0.01	15.41±0.00	15.92±0.01	0.050
C4-7	19.63±0.06	18.73±0.03	18.40±0.16	19.13±0.06	18.08±0.04	17.85±0.15	0.044
C4-8	19.11±0.05	17.92±0.03	17.45±0.03	18.29±0.07	16.98±0.05	16.58±0.04	0.049
C5-1	17.95±0.01	17.12±0.01	16.72±0.01	17.62±0.01	16.82±0.01	16.43±0.02	0.043
C5-2	18.91±0.02	17.68±0.01	17.13±0.02	18.26±0.02	17.09±0.02	16.56±0.02	0.045
C5-3	19.63±0.04	18.94±0.04	18.53±0.06	19.01±0.05	18.43±0.04	18.02±0.06	0.041
C5-4	18.14±0.01	16.76±0.01	16.22±0.01	17.23±0.01	16.01±0.01	15.57±0.01	0.040
C5-5	19.28±0.03	18.56±0.03	18.24±0.05	17.91±0.03	17.12±0.03	16.70±0.05	0.038
N9-1	18.01±0.01	17.14±0.01	16.76±0.01	17.19±0.01	16.40±0.01	16.09±0.02	0.036
N9-2	20.32±0.07	19.13±0.06	18.46±0.06	20.13±0.11	19.04±0.07	18.38±0.10	0.037
U1-1 ^b	18.17±0.02	16.96±0.01	16.42±0.01	17.09±0.02	15.91±0.01	15.38±0.01	0.023
U1-2 ^b	19.19±0.04	17.85±0.01	17.25±0.02	18.66±0.05	17.47±0.02	16.89±0.03	0.025
U1-3 ^b	17.96±0.01	16.08±0.00	15.42±0.00	16.90±0.02	14.96±0.01	14.33±0.01	0.026
U1-4 ^b	18.05±0.02	17.09±0.01	16.64±0.01	16.64±0.01	15.81±0.01	15.40±0.01	0.025
U1-6 ^b	19.32±0.04	18.37±0.02	17.95±0.03	18.06±0.05	17.08±0.03	16.64±0.05	0.027
U1-8 ^b	18.73±0.02	17.05±0.01	16.41±0.01	17.91±0.04	16.47±0.01	15.83±0.01	0.025

^aThe uncertainties included in the table are the intrinsic uncertainties associated with each measurement. Additionally, there is a systematic zeropoint uncertainty of 0.06 mag in the B-band, 0.05 mag in the R_c-band, and 0.05 mag in the I_c-band.

^bPhotometric zeropoints for field U1 were determined relative to field N9. The zeropoint uncertainty for this field is 0.02 mag larger in each band than the other fields. See Section 2.2.2 for details.

calibration of 0.3 mag.

2.3. Spectroscopy

2.3.1. Spectroscopic observations

Spectroscopy was obtained using the Marcario Low Resolution Spectrograph (LRS; Hill et al. 1998) on the 9.2m HET. Table 2 details the instrumental setup. The weather ranged from photometric to some cirrus. Typical image quality was $\sim 2.6''$ FWHM during the 1999-2000 season, and $\sim 2.3''$ FWHM during the 2000-2001 winter, measured on images taken before the spectrum was observed. Additionally, the shape of the point spread function (PSF) was much more regular and symmetric during the second season, as a result of image quality improvements made to the telescope. The only major instrumental change between the two observing seasons was an upgrade of the CCD controller electronics from “version 1” in 1999-2000 to “version 2” in 2000-2001. The version 2 controller provides a much more stable bias and overscan level, faster readout, and lower readout noise.

The typical exposure time was 30 minutes, and multiple observations were made for most of the galaxies to increase the signal-to-noise ratio (S/N) and aid in cosmic ray rejection. Table 5 details the spectroscopic observations.

In total we observed 19 LSB galaxies, two HSB elliptical galaxies (NGC 3872 and UGC 3844) and one HSB post-starburst irregular galaxy (NGC 1569). The HSB observations provide comparisons of old and young stellar populations, respectively. We also observed a K giant star (HD 12402) to use as cross-correlation template for the old stellar populations.

2.3.2. Basic reductions of spectroscopic observations

The spectral data reduction was done using IRAF. The observations spanned about 2.5 years beginning with early science operations of the HET, continuing through the telescope and instrument shake-down periods, and into normal operations. Consequently, we will go into some detail about the basic data reductions, and steps taken to find and correct systematic effects which might be present in the data. Readers not interested in the detailed steps of the basic reduction may skip ahead to Section 2.3.3. The steps of the basic data reduction are as follows:

- 1) bias and overscan subtraction
- 2) dark subtraction
- 3) flatfielding
- 4) cosmic ray cleaning
- 5) wavelength calibration and rectification
- 6) sky subtraction

The dispersion axis in the LRS runs along rows. The version 1 CCD controller electronics, in use from 1999 October - 2000 March, had a variable overscan level, depending on the flux hitting the CCD. If there were rows with high flux such as the spectroscopic trace for bright objects, then the overscan level for those rows would be depressed. Consequently, for bright traces, the overscan had to be subtracted row by row. For faint traces, or uniform illuminations such as with the flatfields, the overscan level was a smooth function of row number, and we subtracted a fit to the overscan, rather than doing it row by row. The version 2 controller produces a very stable overscan level, which is a constant for all rows regardless of the illumina-

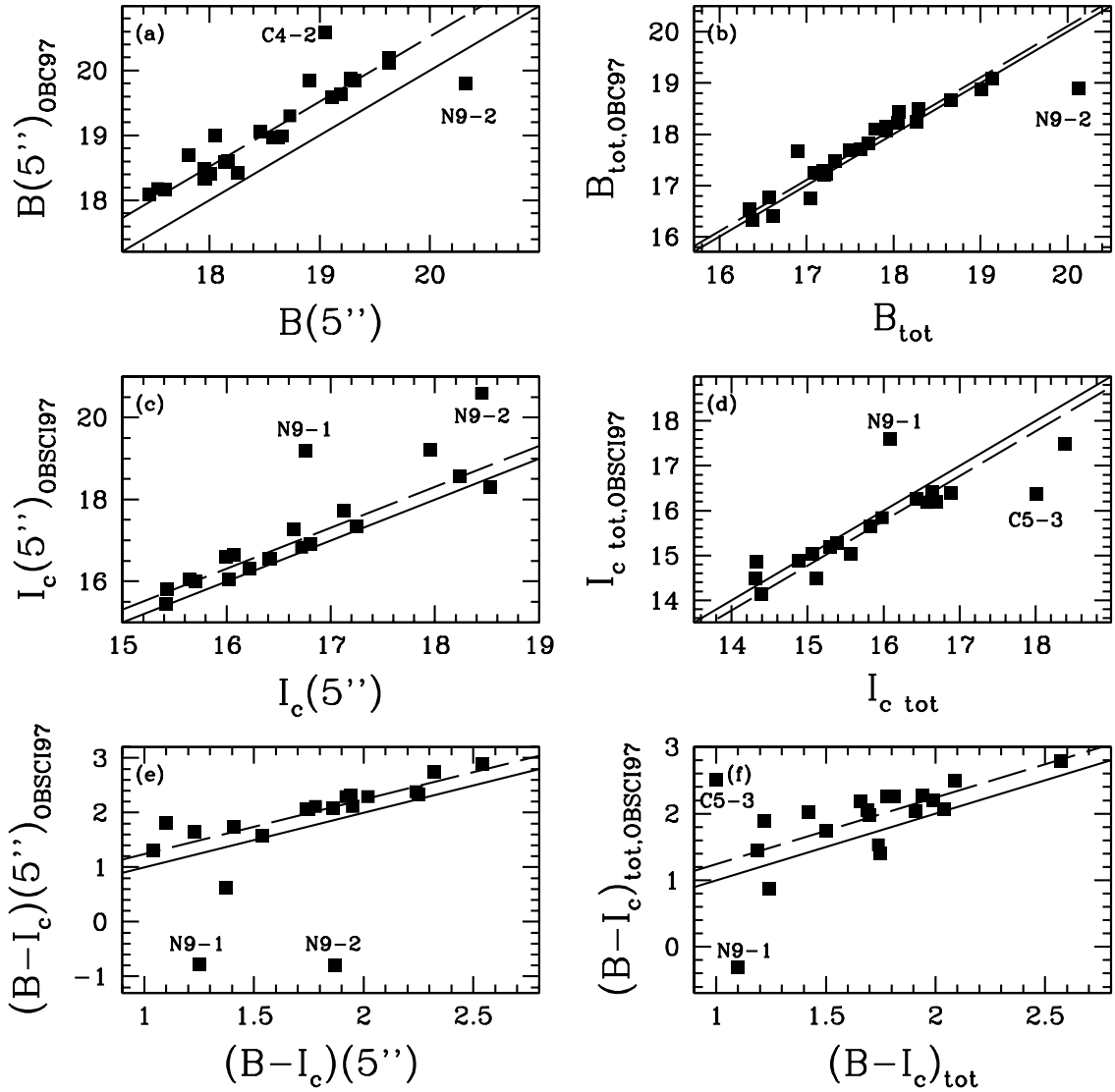


FIG. 1.— Comparison between our photometry and that of OBC97 and OBSCI97. Both datasets have been corrected for galactic extinction. Solid lines denote lines of equality; Dashed lines show the best fit to the zeropoint offset. Typical intrinsic uncertainties for all of the data are less than 0.05 mag, comparable to the size of the boxes. (a) Comparison of B-band magnitudes measured inside apertures of radius 5". The fit to the zeropoint offset gives $\Delta m_{zero} = -0.52 \pm 0.04$ mag (rms=0.19 mag). The two furthest outliers are labelled and were not included in the fit. (b) Comparison of B-band total magnitudes. The zeropoint offset is $\Delta m_{zero} = -0.11 \pm 0.04$ mag (rms=0.21 mag), excluding the two outliers N9-2 and U1-4 (off the plot). The complex surface brightness profiles of these two galaxies were not well fit by OBC97 using single exponential disk fits. (c) Comparison of I-band 5" radius aperture magnitudes. Excluding N9-1 and N9-2, the mean zeropoint offset is $\Delta m_{zero} = -0.31 \pm 0.08$ mag (rms=0.34 mag). (d) The I-band total magnitude comparison. Excluding N9-1, C5-3, and U1-4 (off the plot) gives a best-fit zeropoint offset of $\Delta m_{zero} = 0.23 \pm 0.08$ mag (rms = 0.33 mag). (e) Comparison of $(B-I_c)$ aperture colors. We derive a zeropoint offset of $\Delta(B-I_c)(5'') = -0.24 \pm 0.07$ mag (rms=0.29 mag). The two labelled outliers were not included in the fit. (f) Comparison of the total $(B-I_c)$ colors. The zeropoint offset is the same as for the aperture colors: $\Delta(B-I_c)(5'') = -0.24 \pm 0.07$ mag (rms=0.30 mag), excluding the two labelled points.

tion.

Mean bias frames were produced each month by combining all bias (zero exposure time) images taken on nights when science data was obtained. These images were over-scanned, then averaged together, with sigma clipping to eliminate cosmic rays. The coadded bias image was then fit with a low-order surface, and this fit was subtracted from all the science data for that month. The mean of the fit was about 1.4 ADU. Month to month variations were 0.1 ADU.

Flatfield correction was done using lamp flats to correct small scale pixel-to-pixel variations, and using twilight spectra to correct for the slit illumination in the spatial dimension. Mean lamp flats were derived for each night, and checked against each other for variations, which were negligible. While fringing is evident redward of ~ 7000 Å, it is not seen to vary in the flats over the course of a month. There is some variation between months, caused by shifts in the slit position with respect to the image field center, and the corresponding wavelength range hitting the CCD.

TABLE 5
HET SPECTROSCOPIC OBSERVATIONS

Name	Exposure Time ^a	N _{obs} ^b	PA slit ^c	Dates of observations
P1-3	1195	1	46	Nov 30, 2000
P6-1	4200	3	45	Dec 21,22(×2), 2000
P9-4	3600	2	41	Nov 23,24, 2000
C1-2	2014	2	-66	Dec 10, 1999(×2)
C1-4	5160	3	-67	Nov 11, 1999(×2);Mar 11, 2000
C3-2	3300	2	-67	Nov 10, 1999; Dec 7, 1999
C4-1	2770	2	-67, 67	Nov 21, 2000; Jan 26, 2001
C4-5	3750	2	-67, 68	Nov 12, 1999; Mar 6, 2000
C5-3	6700	4	-68, 67	Nov 14, 1999; Dec 14,17, 1999; Mar 13, 2000
C5-5	1666	1	-69	Nov 30, 2000
C6-1	1200	1	-67	Nov 24, 2000
C8-3	4800	4	-67, 67	Dec 22, 2000(×2); Jan 27, 2001(×2)
N3-1	3300	2	-49, 47	Dec 10, 1999; Mar 12, 2000
N9-1	3600	2	-75	Nov 13, 1999; Dec 8, 1999
N9-2	5200	3	-76, 76	Dec 13, 1999; Mar 3, 2000
N10-2	3600	2	-66	Dec 6, 1999; Dec 7, 1999
N10-4	5280	3	-66, 66	Dec 11, 1999; Mar 12,13, 2000
U1-4	3600	2	-62	Dec 13,14, 1999
U1-8	1800	2	-60	Dec 8,10, 1999
NGC 3872	900	1	-59	Dec 7, 1999
UGC 3844	600	1	-82	Dec 7, 1999
NGC 1569	600	1	8	Nov 10, 2000

^aTotal exposure time for all observations, in seconds

^bNumber of individual exposures

^cMeasured in degrees North through East; always parallactic

The lamp flats taken for each month were combined into a single master flat. The rms uncertainty in these master flats is about 0.1% redward of 6000 Å, increasing slowly blueward to 0.15% at 4800 Å.

Spectra of the sky taken during morning twilight were used to determine the slit illumination. The twilight flats were averaged together, then collapsed along the spectral dimension leaving a one dimensional “image” of the slit. This spatial profile was then applied to the lamp flat to correct for the large scale response of the instrument, along the slit. The way the HET operates, the spherical primary mirror is not moved during an observation. Instead, tracking is accomplished by moving the entire Prime Focus Instrument Package (PFIP) relative to the primary mirror much in the way the Arecibo 305m radio telescope is pointed. As objects are tracked across the mirror, the pupil entering the instrument changes and, consequently, so does the slit illumination. We found that the twilight flats taken with the PFIP location fixed often did not represent the slit illumination during our science exposures. The gross vignetting pattern of the telescope optics was represented, but small gradients remained. These gradients were corrected as part of the sky subtraction procedure, described below.

Cosmic ray rejection was done using an IRAF script called `speccrrej` (a prototype of a task which is planned for the Gemini IRAF package). This task makes a two dimensional model of the longslit spectrum, sensitive to features larger than ~ 30 square pixels. It does a fairly good job of simulating the spectrum, as well as most of the sky lines. However, sharp features are not modeled, and show up in the difference image. Most of these features are cosmic rays, though strong skylines and sometimes strong emission lines or deep absorption troughs are also flagged. The cosmic ray masks were all checked manually to make sure that real spectral features were not flagged. The flagged cosmic rays were then replaced by

the values from the model spectrum. Pixels affected by cosmic rays were added to the bad pixel masks for each exposure.

Spectral arc lamps (Ne and HgCdZn) were observed each night with our setup. We used the IRAF tasks `identify`, `reidentify`, and `fitcoords` to establish the spectral dispersion function in the two dimensional spectra. There were 34 lamp lines used over the full wavelength range, and the fifth order polynomial fits typically had an RMS scatter of 0.2 Å. There were small (less than 2 Å) wavelength offsets found for the skylines in many of the science exposures, caused by a shifting of the slit position between setups. These shifts caused a wavelength shift in the dispersion function, but no change in its shape. The wavelengths of several strong skylines (OII λ 5577, OII λ 6300) were used to correct for these offsets. The `identify` task was also used to find the spectral trace along the spatial dimension. In cases where the trace of a galaxy was too faint to be seen, the fit for a brighter object observed the same night was used instead. We then rectified the two dimensional spectra.

Prior to sky subtraction, we checked the quality of the spatial illumination correction for each spectrum, by measuring the flux of several strong sky lines along the slit. The sky level should be constant along the slit, but due to the varying illumination of the HET image pupil, the simple twilight flatfield was not always effective. In these cases, we fitted any residual illumination gradient with a smooth low order function, and divided it out. Sky regions bracketing the spectral trace were averaged, and then subtracted from the full 2D spectrum. This produced good results, except near the OII λ 5577, NaD λ 5895, and OII λ 6300 skylines, which were simply interpolated over. These bad regions are marked in the spectra presented in Section 3.

2.3.3. Spectral extraction, coaddition, flux calibration

We extracted the spectra in apertures of length r_e (thus including the signal within $r_e/2$ of the center, rounding off to the nearest integer pixel), by simply summing the appropriate rows. Since the galaxies cover a wide range of distances, the fixed slit width of $2''$ will cover a varying fraction of the galaxy disks. However, since no good spectral gradient data exist for these types of galaxies, we choose to simply note this fact and not attempt any corrections for it. The galaxies C3-2 and C4-1 did not have exponential scale lengths reported in OBC97. We chose the apertures for these galaxies based on their light profiles along the slit and to optimize the S/N; we use an aperture length of $6''$ for C3-2, and $11''$ for C4-1.

A special correction had to be made for the data from 1999 November. During the first month of science observations with the telescope, a glass membrane pellicle was used as part of the telescope guiding system. This membrane caused a fringe pattern to appear in the data, with a fringe wavelength of 300-400 pixels, and a strength and location that varied from one exposure to the next. For each of the galaxies observed in 1999 November, we obtained at least one additional spectrum during a later month. To remove the fringe pattern from the data, we fit the continuum, and normalized the spectrum by this fit. We then multiplied the normalized spectrum with the average continuum fit from the data not affected by the fringing problem.

Most of the galaxies had multiple observations, often taken several months apart. Before coadding the spectra, we corrected the wavelength scales to a consistent velocity with respect to the sun. The spectra were then averaged.

Each night of science observations, a spectrophotometric standard star was observed. The relative flux response of the instrument is very stable (with the exception of the data from 1999 November), and we based the relative flux calibration on all the standard stars observed during an observing season. For the 1999-2000 season, we used 15 standard star observations, and for the 2000-2001 season we averaged 7 observations. The stars observed were: HD 84937, HD 19445, HZ 4, HZ 44, Feige 34, Feige 66, Feige 67, Gl 191B2B, Hiltner 600, BD+25 3941, and BD+26 2606. The observed spectral energy distributions (SED) were scaled to account for grey extinction due to cirrus, and then fit with a sixth order polynomial, with an RMS deviation of less than 0.1%. When the different observations are scaled to the same value at 5800 \AA , the full range of measurements at both 4800 \AA and 7150 \AA spans 0.25%, which we take to be the maximum expected relative uncertainty over large wavelength ranges. We then applied these relative flux calibrations to all the coadded spectra.

In parallel with the spectral reductions and extractions, variance spectra were produced. These are derived by first assuming poisson noise from the sky and object counts, then folding in readout noise, flat-fielding uncertainty, the effects of rectification and extraction, and finally the co-addition of spectra.

2.3.4. Redshifts

Redshifts are derived in two separate ways, (1) from cross-correlation with absorption line templates and (2) from measurements of the emission line wavelengths.

We used the IRAF task `xcor` to compute the cross-correlations for galaxies showing stellar absorption fea-

tures, with an observation of HD12402 (spectral type K1III) as the stellar template. The restframe wavelength range used for the computation was $4300 \text{ \AA} - 6500 \text{ \AA}$ for galaxies with no significant $H\beta$ emission (C1-2, C1-4, U1-8, N3-1). For galaxies with $H\beta$ emission, the cross-correlation was performed over the range $5000 \text{ \AA} - 6000 \text{ \AA}$, which still includes several strong absorption features. The uncertainties determined by the `xcor` task were 60 km/s for the galaxies without $H\beta$ emission and 75 km/s for the systems with both absorption and emission features.

Redshifts for the emission line galaxies were based on positions of the lines $H\beta$, $[O \text{ III}]\lambda\lambda 4959, 5007$, $H\alpha$, $[N \text{ II}]\lambda 6584$, and $[S \text{ II}]\lambda\lambda 6717, 6731$. We take the mean velocity of all the strong lines as the systemic velocity, and the rms scatter as the uncertainty in the velocity. This uncertainty was typically $\sim 30 \text{ km/s}$ for galaxies with at least four emission lines detected.

For the galaxies where we measure redshifts from both the emission lines and stellar absorption features, the two measurements were always consistent with no velocity offset, to within the uncertainties. We transform the redshifts into the heliocentric reference frame. The measured redshifts are listed in Table 7. We list the emission line redshifts when available, otherwise the absorption line redshifts are shown.

2.3.5. Emission line measurements

Emission line strengths are measured using the IRAF task `fitprofs`. Nearby lines are measured simultaneously, using the `deblend` option, and constraining the fit to have a single width for all the nearby lines. We use the variance spectra to estimate the ‘‘inverse gain’’ parameter, used by `fitprofs` in its Monte Carlo estimation of the uncertainties.

In many cases, the measurement of the $H\beta$ emission strength is clearly affected by underlying stellar absorption. We correct this individually for each galaxy. The adopted correction procedure is as follows. The wavelength coverage of the emission line is defined at its base, the widest point. The continuum level is defined with a straight line between the two sides of the base. The emission line flux and equivalent width are then measured above this continuum level. The V1999 single burst stellar population model spectra, convolved to our instrumental resolution, are then used to estimate the effect of the underlying stellar absorption profile on the emission measurements. For each galaxy, we find the model which best fits the absorption lines in the restframe wavelength range $4800 \text{ \AA} < \lambda < 5450 \text{ \AA}$. We also determine what range of model ages and metallicities brackets a reasonable fit to the spectrum. The fits are all done by eye. We define a continuum level on the models, by drawing a straight line between the model values at either side of the emission line wavelength interval, and measure the equivalent width of absorption below this level. We then combine the equivalent width of absorption seen in the models with the equivalent width of emission measured above the interpolated continuum in the data to get a corrected $H\beta$ equivalent width measurement. Finally, we scale the $H\beta$ flux measurement by the ratio of the corrected to uncorrected equivalent widths to determine the total emission line flux corrected for underlying absorption. Examples

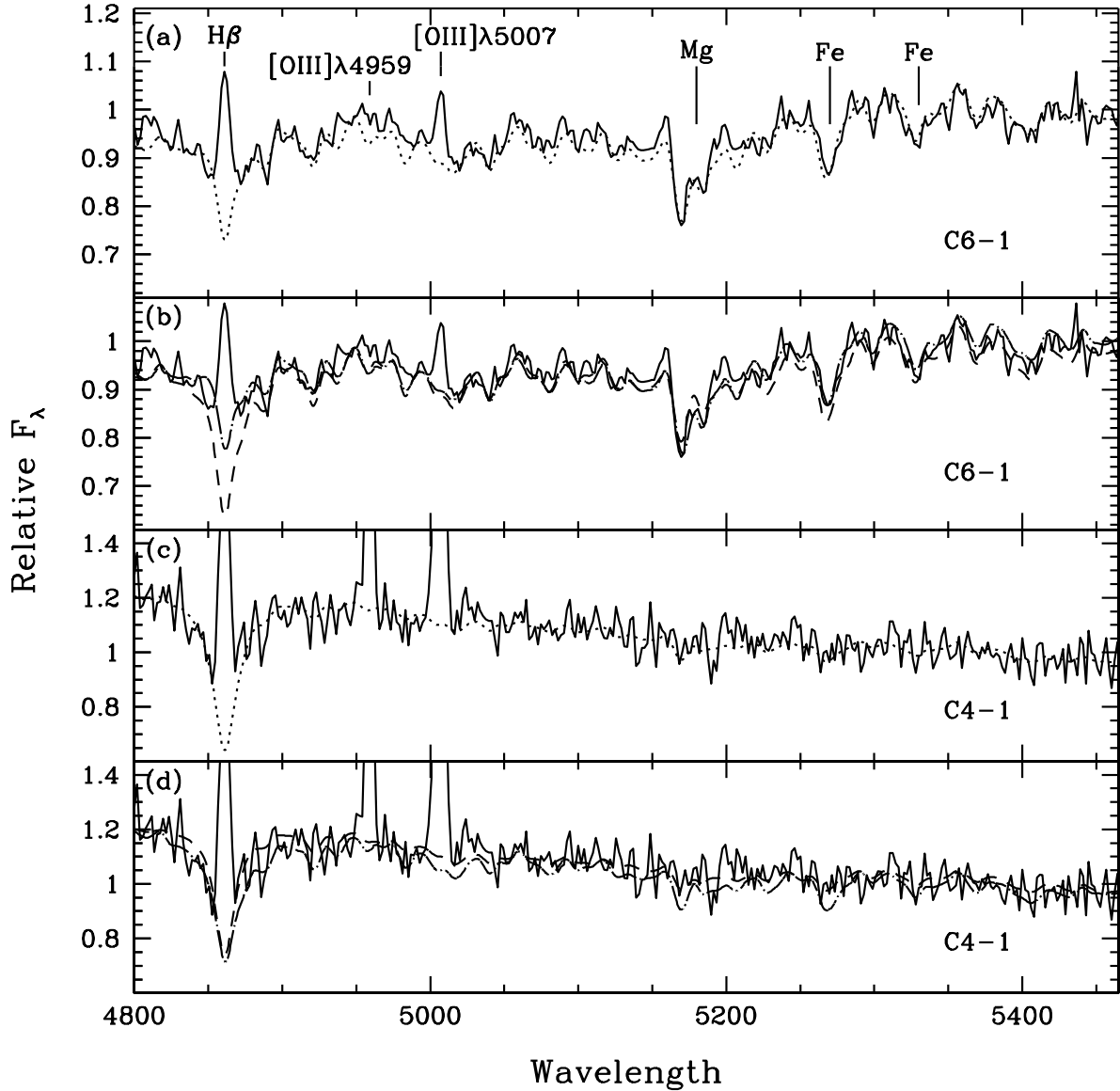


FIG. 2.— Correction of the H β emission line strengths for underlying H β absorption. Solid lines – observed spectra; dotted lines – best fitting model; dashed lines – youngest acceptable model; dot-dashed lines – oldest acceptable model. The strongest emission and absorption features in this wavelength region are labelled in panel (a). (a) C6-1 with the best fitting model, age=3.2 Gyr, [Fe/H]=−0.4. (b) C6-1 with oldest (age=13.2 Gyr, [Fe/H]=−0.7) and youngest (age=1.0 Gyr, [Fe/H]=0.0) acceptable models. (c) C4-1 with the best fitting model, age=250 Myr, [Fe/H]=0.0. (d) C4-1 with oldest (age=630 Myr, [Fe/H]=0.0) and youngest (age=100 Myr, [Fe/H]=0.0) acceptable models. Note that the depth of the H β absorption reaches a maximum for an SSP of 200 Myr, and so appears weaker in both the older and younger models.

of this technique applied to two of the galaxies are shown in Figure 2. Table 6 lists the measured uncorrected H β equivalent widths as well as the parameters of the best fitting, youngest, and oldest models, and their corresponding absorption equivalent width corrections.

We list two sets of uncertainties for the H β fluxes in Table 7. The first set are the random uncertainties derived from the fit to the emission line flux, the same as for the other emission lines. Additionally, we include a set of uncertainties showing the range of the absorption corrections consistent with the reasonable fitting models.

The V1999 models, which use an empirical spectral library, are limited in their ability to model young ages

at sub-solar metallicities. We also investigated using the Starburst99 models (Leitherer et al. 1999), which cover very young ages at both solar and 1/20 solar metallicity. However, the narrow wavelength coverage of their models does not permit us to fit the metallic absorption features at longer wavelength, which provide the most constraint on the range of reasonable models.

Telluric absorption in the atmospheric B band ($\lambda \simeq 6840$ Å) affected our line strength measurements for two galaxies. The [N II] λ 6584 line was absorbed in the galaxy C5-3. Nebular physics predicts [N II] λ 6584 = 2.95 · [N II] λ 6548 (Osterbrock 1989, p. 61). For the 9 LSB galaxies with emission and where strong H α does not make it impossi-

TABLE 6
H β EQUIVALENT WIDTH CORRECTIONS

Name	EW(H β) _{em} (Å)	best-fit model ^a			max EW(H β) model ^b			min EW(H β) model ^c		
		age (Gyr)	[Fe/H]	EW(H β) _{abs} (Å)	age (Gyr)	[Fe/H]	EW(H β) _{abs} (Å)	age (Gyr)	[Fe/H]	EW(H β) _{abs} (Å)
C3-2	2.0±0.1	1.58	0.2	-1.3	0.63	0.0	-1.0	11.0	-0.7	-1.9
C4-1	7.5±0.6	0.25	0.0	-2.2	0.10	0.0	-1.8	0.63	0.0	-2.2
C4-5	0.9±0.3	0.79	0.0	-1.2	0.40	0.0	-1.0	1.58	0.0	-1.5
C6-1	2.7±0.3	3.16	-0.4	-1.6	1.00	0.0	-1.3	13.2	-0.7	-2.4
C8-3	3.4±0.4	0.50	0.0	-1.1	0.10	0.0	-0.9	0.79	0.0	-1.2
N10-2	1.3±0.1	7.94	-0.4	-1.0	1.00	0.2	-0.8	17.4	-0.7	-1.4
N9-1	11.5±0.3	0.40	0.0	-2.6	0.03	0.0	-1.7	1.00	0.2	-2.9
N9-2	27.7±0.9	0.25	0.0	-4.4	0.10	0.0	-3.4	0.63	0.0	-4.5
P1-3	7.2±0.4	1.00	0.0	-1.3	0.40	0.0	-1.0	6.31	-0.7	-1.9
P6-1	1.3±0.2	3.16	-0.4	-1.0	1.00	0.2	-0.8	11.0	-0.7	-1.4
U1-4	2.6±0.1	0.63	0.0	-2.0	0.50	0.0	-1.9	0.79	0.0	-2.3

^aParameters for the “best-fit” stellar population model and the equivalent width of H β absorption over the narrow wavelength region for which we measure emission. The “best fit” as well as the determination of the maximum and minimum reasonable corrections were done by eye. See Section 2.3.5 for details.

^bThe model which requires the largest correction to the H β equivalent width, but is still a reasonable fit to the other absorption features in the spectrum. This is typically the youngest, highest metallicity, marginally acceptable model.

^cThe model which requires the smallest correction to the H β equivalent width, but is still a reasonable fit to the other absorption features in the spectrum. This is typically the oldest, lowest metallicity, marginally acceptable model.

ble to measure the [N II] λ 6548 line, the mean [N II] λ 6584 / [N II] λ 6548 ratio is 2.9 ± 0.9 . We use the measured value of [N II] λ 6548 in C5-3 and the theoretical ratio to calculate the non-absorbed [N II] λ 6584 strength (0.27 ± 0.08 relative to H β). For the galaxy N9-1, [N II] λ 6548,6584, and H α all suffered some absorption. For this galaxy, we estimate the additional uncertainty on the [N II] λ 6584/H α ratio to be 10%, and we also likely underestimate the H α /H β ratio by 10%. The uncertainties on the relative emission line fluxes listed for N9-1 in Table 7 have been adjusted to account for this. In the following the [N II] λ 6584/H α ratio is simply called [N II]/H α .

We correct the relative emission line strengths for galactic reddening using the Cardelli extinction law (eqs. 3a and 3b in Cardelli et al. (1989)), with the galactic reddening measurements from Schlegel et al. (1998) as listed in Table 1. $R_V=3.1$ is assumed. The amount of galactic reddening is variable across the field of NGC 1569. We follow Kobulnicky & Skillman (1997) and adopt the value of 0.5 mag (Burstein & Heiles 1982), so that we may make a direct comparison to their results (see section 2.3.7). We have not corrected the emission line strengths for dust reddening internal to the galaxies. We discuss the dust content of these galaxies in Section 7. The emission line ratios used for ionization determination and abundance analysis (e.g. [O III] λ 5007/H β and [N II]/H α) utilize lines with small wavelength separations, and these ratios are not affected by reddening at the level seen in these galaxies. The H α equivalent widths are also corrected for the effects of cosmological expansion, $EW(\lambda_{rest})=EW(\lambda_{obs}) \cdot (1+z)$ (see Peterson 1997, page 156).

We present the measured emission line strengths as well as the equivalent width of H α in Table 7. These data do not have an absolute flux calibration. There are several reasons for this. As objects are tracked across the sky by moving the HET prime focus instrument platform, the region of the primary mirror seen by the instrument changes. Furthermore, not all of the primary mirror is seen all the time, and thus the telescope throughput varies during an object track. Additionally, the PSF at the spec-

trograph entrance slit changed (sometimes dramatically increasing in size) during exposures, and some of the observations were taken through cirrus clouds. Consequently, we tabulate only relative fluxes, and for convenience we have scaled them to an H β flux of 1. For Table 7, we list both the random and systematic uncertainties on the scaled H β flux, rather than incorporating these into the uncertainties of the other flux measurements and listing line ratios. The uncertainties on H β are incorporated into the [O III] λ 5007/H β ratios plotted in Figure 6 and the H α /H β ratios shown in Figure 11.

2.3.6. Absorption line indices

We have measured the strength of the stellar absorption lines H β , Mgb, Fe5270, and Fe5335 using the line index definitions of the Lick/IDS system (Worthey et al. 1994). Several calibrations were made to match our observations to the characteristics of the IDS spectrograph and put our measurements onto the Lick system. Before measuring the indices, it was necessary to match our spectra to the instrumental resolution of the IDS spectrograph. We convolved our spectra with a wavelength dependant Gaussian to accomplish this. Additionally, stellar features in galaxy spectra are broadened by the internal velocity dispersion of the galaxies, and this broadening will have an effect on the measured strength of the line indices. To facilitate comparison with stellar population models, we correct our observations to the equivalent strength for a system with zero velocity dispersion, following the method of Davies, Sadler, & Peletier (1993): we determined the correction by taking a spectrum of a K giant star, already convolved to the IDS resolution, and convolving it with Gaussians of increasing velocity width, in 25 km/s increments, up to 400 km/s. We measured the index strengths on this suite of stellar spectra, and used the offsets between each velocity width and the unbroadened spectrum to correct the galaxy measurements. Since we do not actually resolve the velocity dispersion of the LSB galaxies, we assume a value of 75 km/s. The correction factors by which the measurements are multiplied are as follows: H β (1.004);

TABLE 7
SPECTROSCOPIC DATA

Name	S/N ^a	cz_{hel} ^b	M_B ^c	Absorption Line Indices			Emission Line Fluxes							
				H β	Mgb	< Fe >	EW(H α)	H β ^d	[OIII] λ 5007	[NII] λ 6548	H α	[NII] λ 6584	[SII] λ 6717	[SII] λ 6731
P1-3	19	17505	-19.67	...	0.9 \pm 0.4	1.4 \pm 0.4	31 \pm 1	1.00 \pm 0.05 ^{+0.07} _{-0.04}	1.48 \pm 0.05	0.20 \pm 0.04	3.44 \pm 0.07	0.70 \pm 0.06	0.89 \pm 0.05	0.65 \pm 0.05
P6-1	34	10891	-18.53	...	3.1 \pm 0.2	2.1 \pm 0.2	8.0 \pm 0.2	1.00 \pm 0.17 ^{+0.15} _{-0.09}	...	0.75 \pm 0.07	5.0 \pm 0.1	2.3 \pm 0.1	1.70 \pm 0.09	1.13 \pm 0.08
P9-4	7	4108	-14.67	73 \pm 7	1.00 \pm 0.06	...	3.1 \pm 0.1	0.04 \pm 0.04	3.76 \pm 0.09	0.30 \pm 0.05	0.56 \pm 0.06
C1-2	19	4615	-16.26	2.0 \pm 0.4	3.0 \pm 0.4	2.2 \pm 0.3
C1-4	70	3883	-17.35	1.9 \pm 0.1	3.5 \pm 0.1	2.50 \pm 0.09
C3-2	41	4528	-17.63	...	2.4 \pm 0.2	2.0 \pm 0.2	11.0 \pm 0.1	1.00 \pm 0.06 ^{+0.18} _{-0.09}	...	0.33 \pm 0.04	3.84 \pm 0.05	1.49 \pm 0.04	0.82 \pm 0.05	0.76 \pm 0.06
C4-1	14	4927	-16.48	...	1.0 \pm 0.5	0.8 \pm 0.5	30 \pm 2	1.00 \pm 0.07 ^{+0.06} _{-0.04}	1.53 \pm 0.07	0.09 \pm 0.04	2.64 \pm 0.09	0.25 \pm 0.05	0.56 \pm 0.06	0.39 \pm 0.05
C4-5	23	4633	-16.01	...	1.1 \pm 0.3	1.7 \pm 0.3	6.3 \pm 0.3	1.00 \pm 0.25 ^{+0.12} _{-0.13}	0.5 \pm 0.1	0.47 \pm 0.13	2.9 \pm 0.1	0.9 \pm 0.1	1.3 \pm 0.1	0.9 \pm 0.1
C5-3	12	12944	-17.21	...	0.9 \pm 0.6	1.0 \pm 0.5	63 \pm 1	1.00 \pm 0.06	3.78 \pm 0.09	0.09 \pm 0.03	3.53 \pm 0.08	0.27 \pm 0.08 ^e	0.62 \pm 0.05	0.41 \pm 0.04
C5-5	5	5473	-16.49	25 \pm 2	1.00 \pm 0.28	4.3 \pm 0.4	5.8 \pm 0.4
C6-1	22	25035	-20.13	...	3.1 \pm 0.3	2.2 \pm 0.3	14.4 \pm 0.6	1.00 \pm 0.12 ^{+0.17} _{-0.08}	...	0.65 \pm 0.06	4.3 \pm 0.1	1.96 \pm 0.09
C8-3	17	3648	-15.91	...	1.1 \pm 0.4	1.0 \pm 0.4	16.3 \pm 0.6	1.00 \pm 0.12 ^{+0.03} _{-0.03}	3.2 \pm 0.2	0.25 \pm 0.06	3.2 \pm 0.1	0.31 \pm 0.07	0.74 \pm 0.09	0.42 \pm 0.07
N3-1	72	25222	-19.67	1.7 \pm 0.1	4.7 \pm 0.1	3.03 \pm 0.09
N9-1	38	15128	-19.38	...	1.6 \pm 0.2	...	41 \pm 1	1.00 \pm 0.02 ^{+0.02} _{-0.07}	0.71 \pm 0.02	0.12 \pm 0.01	2.88 \pm 0.02	0.80 \pm 0.01	0.81 \pm 0.02	0.57 \pm 0.02
N9-2	13	73629	-19.84	...	1.3 \pm 0.6	1.3 \pm 0.5	...	1.00 \pm 0.03 ^{+0.00} _{-0.04}	1.09 \pm 0.03
N10-2	38	20668	-20.69	...	2.8 \pm 0.2	2.2 \pm 0.2	8.1 \pm 0.2	1.00 \pm 0.11 ^{+0.17} _{-0.07}	0.33 \pm 0.08	0.70 \pm 0.09	3.80 \pm 0.08	1.90 \pm 0.06	0.57 \pm 1.1 ^f _{\pm0.07}	0.32 \pm 0.9 ^f _{\pm0.07}
N10-4	8	7447	-16.20	7 \pm 1
U1-4	53	3416	-16.86	...	1.0 \pm 0.2	0.8 \pm 0.1	11.9 \pm 0.2	1.00 \pm 0.05 ^{+0.06} _{-0.03}	1.13 \pm 0.04	0.11 \pm 0.02	2.18 \pm 0.03	0.32 \pm 0.03	0.57 \pm 0.02	0.43 \pm 0.02
U1-8	35	32123	-20.27	2.0 \pm 0.3	3.0 \pm 0.2	2.2 \pm 0.2
NGC3872	153	3114	-21.83 ^g	1.47 \pm 0.05	5.04 \pm 0.05	2.83 \pm 0.04
UGC3844	38	3192	-20.77 ^g	1.5 \pm 0.2	4.6 \pm 0.2	3.5 \pm 0.2
NGC1569 ^h	120	-96	-17.23 ^g	...	0.68 \pm 0.07	0.71 \pm 0.06	95.6 \pm 0.6	1.00 \pm 0.00	5.96 \pm 0.01	0.06 \pm 0.00	3.92 \pm 0.00	0.14 \pm 0.00	0.20 \pm 0.00	0.14 \pm 0.00

^aSignal-to-noise per Å of the continuum, measured between 5050Å and 5150Å.

^bHeliocentric radial velocity: Based on emission lines, if present. Otherwise based on cross-correlation with absorption line template.

^cTotal absolute magnitude: Based on our photometry, if available, otherwise from OBC97. Assuming $H_0=75 \text{ kms}^{-1}\text{Mpc}^{-1}$, and distances based on redshifts in the CMB reference frame.

^dEmission line fluxes are normalized to $f(H\beta)=1$. The first set of uncertainties on H β are the random uncertainties and the second set are the range of absorption corrections consistent with the stellar population models. If no second set is listed, the correction is negligible compared to the uncertainty due to random error.

^eCalculated from [NII] λ 6548 \times 2.95

^fLower value is the intrinsic uncertainty, upper value is a systematic uncertainty, caused by poor flux calibration at the extreme red end of the spectrum. See Figure 6.

^gData from the LEDA database (<http://leda.univ-lyon1.fr>), and adjusted to $H_0=75 \text{ kms}^{-1}\text{Mpc}^{-1}$.

^hUncertainties listed as 0.00 are less than 0.005.

Mgb (1.02); Fe5270 (1.02); Fe5335 (1.04). The correction is such that for galaxies whose true velocity dispersion is larger than we have assumed (75 km/s), we will derive index values which are weaker than the actual values for that stellar population if it were observed with zero intrinsic velocity dispersion. If the actual velocity dispersion of the galaxy is 150 km/s instead of 75 km/s, then we will systematically underestimate the H β strength by 1%, the Mgb strength by 3%, the Fe5270 strength by 5%, and the Fe5335 strength by 8%. For N3-1 and the two elliptical galaxies we correct for a velocity dispersion of 250 km/s. NGC 3872 has a velocity dispersion of $\sigma=243$ km/s (Davies et al. 1987), while we simply assume 250 km/s for UGC 3844 and N3-1. The correction factors are H β (1.02); Mgb (1.17); Fe5270 (1.16); Fe5335 (1.36).

Uncertainties for the index strengths are derived from the variance spectra. Essentially, we use poisson statistics on the flux in both the line and continuum bandpasses, additionally accounting for the contribution caused by the readout noise, and flatfielding, relative flux calibration, and sky subtraction uncertainties.

In several cases, residuals from imperfect subtraction of strong skylines (O λ 5577, NaD) fall in the index bandpasses. When the residuals lie in the index continuum bandpasses, we correct the residuals by interpolating over the affected region, using values determined from comparison with the V1999 stellar population models. Observations corrected in this way are N10-2 (Mgb red continuum, Fe5270 blue continuum), N3-1 (Mgb blue continuum), U1-8 (Fe5270 red continuum), and C6-1 (Mgb blue continuum). In some cases, the sky residuals lie on the absorption line itself, and this cannot be corrected. Both Fe5270 and Fe5335 are affected in N9-1. The Fe5335 line is affected for C5-3 and U1-8 while the Fe5270 line is affected for P1-3. There are strong correlations between Fe5270, Fe5335, and $\langle \text{Fe} \rangle$ (defined as $\langle \text{Fe} \rangle = (\text{Fe5270} + \text{Fe5335}) / 2$). Using the LSB galaxy data not affected by the large sky subtraction uncertainties, we derived the relation $\text{Fe5335} = (1.14 \pm 0.08) \cdot \text{Fe5270} - (0.74 \pm 0.24)$. We use this relation to correct the affected indices.

Intrinsic emission from these galaxies could affect the line indices Mgb and H β . Goudfrooij & Emsellem (1996) have found that the [NI] emission doublet at 5199 Å can affect the strength of the Mgb index in early-type galaxies which have ionized gas emission. Many of these LSB galaxies have emission lines, so this is cause for concern. However, the [NI] doublet is strong in LINERs, not H II regions, and none of these galaxies show line ratios consistent with this type of nuclear activity (see Section 4). Additionally, since these are integrated spectra, rather than nuclear spectra, we do not expect the Mgb index to be contaminated. The H β index, on the other hand, is certainly affected by emission in all but three of the galaxies in our sample. For one more galaxy (U1-8), the H β emission must be small. The observed wavelength range for U1-8 does not include either H α or [O II] λ 3727. While the spectrum is dominated by absorption features, there is a small amount of emission seen at [O III] λ 5007 which suggests that the H β absorption index will also be affected by emission. The equivalent width of [O III] λ 5007 emission is 1.2 ± 0.4 Å. Trager et al. (1999) determine the relation between [O III] λ 5007 and H β emission strength in

elliptical galaxies to be $\text{EW}(\text{H}\beta) \simeq 0.6 \cdot \text{EW}([\text{O III}]\lambda 5007)$. This ratio is metallicity sensitive, and will tend to decrease with decreasing metallicity. The integrated galaxy spectra studied by Kobulnicky, Kennicutt, & Pizagno (1999) show ratios as low as $\text{EW}(\text{H}\beta) \simeq 0.25 \cdot \text{EW}([\text{O III}]\lambda 5007)$ at the metallicity appropriate for U1-8 ($\simeq 0.4 Z_{\odot}$; see Figure 7). We therefore apply a correction to the H β absorption index for U1-8 of 0.5 ± 0.3 Å.

For the 15 LSB galaxies with strong emission lines, a correction of the H β absorption index for the H β emission (and its uncertainty) would be a significant fraction of the H β absorption strength. Consequently, we do not present this absorption index for any of the other LSB galaxies.

The absorption line strengths of H β , Mgb, and $\langle \text{Fe} \rangle$ are presented in Table 7.

2.3.7. Comparison to literature data

Our sample has a very wide range in radial velocities, from 3000 km/s to more than 60,000 km/s ($z=0.2$). These same galaxies have been observed in the H I survey of O’Neil et al. (2000a), who give detections for twelve of them. We find several discrepancies between our redshift measurements and the redshifts reported in that survey. The H I survey only covered the velocity space out to 13,000 km/s so more distant objects would not have been detected. However, for the galaxies P1-3, C6-1, and N9-2, lower H I redshifts must have been attributed incorrectly to these higher redshift galaxies. The H I detections for P1-3 and C6-1 can be explained by beam confusion. At 21cm, the beam-size of the Arecibo 305m radio telescope is almost 3’, and both of these galaxies appear in the sky at a projected distance of less than 3’ from a large spiral galaxy at lower redshift. The H I detection ascribed to P1-3 is probably NGC 7631 ($cz_{\text{HI}} = 3746$ km/s; $cz_{\text{opt}} = 3741$ km/s (Falco et al. 1999; hereafter UZC), and the detection ascribed to C6-1 is probably NGC 2595 ($cz_{\text{HI}} = 4322$ km/s; $cz_{\text{opt}} = 4320$ km/s, UZC). The mis-identification also explains why these galaxies appeared to have extreme M_{HI}/L ratios, and lie more than 5σ from the I band Tully-Fisher relation (O’Neil et al. 2000a). Similar cases of beam confusion explain discrepant measurements for the lower redshift LSB galaxies as well. The detection ascribed to C8-3 is probably UGC 4308 ($cz_{\text{HI}} = 3570$ km/s; $cz_{\text{opt}} = 3566$ km/s, UZC), and the detection of C5-5 is more likely UGC 4416 ($cz_{\text{HI}} = 5524$ km/s; $cz_{\text{opt}} = 5555 \pm 45$ km/s, UZC).

There are also cases where the optical and H I redshifts are discrepant, but beam confusion is not obviously the reason: N9-2 (listed above), C4-1, C1-2, and possibly P9-4 (where the optical and H I velocities differ by 3σ). C1-2 in particular is a hard case to explain the H I detection. The difference between optical and H I velocities is ~ 3900 km/s so the H I detection is clearly a different object. However, there are no obvious candidates within 15’ of the pointing, which lie at the redshift of the H I detection, and very few bright objects in that area for which optical redshifts were not obtained by the redshift survey of Zabludoff & Mulchaey (2000). We are forced to conclude that either the H I observation was errant, due to either noise or incorrect pointing, or that there are very large H I clouds with little associated optical light. Two starless objects have been found by the HIPASS survey (Kilborn et al. 2000; Ryder et al. 2001) but the first one had only a 4

km/s velocity width, and the second was associated with the galaxy NGC 2442, so neither one is a good analogue.

The remaining four galaxies, C5-3, P6-1, N10-4, and U1-4 are in good agreement, less than 1σ separating the optical and H I measurements.

Recently, Chung et al. (2002) used the VLA to map the H I around the galaxies P1-2, P1-3, C6-1, C4-1, and C4-2 from the OBC97 sample. They also discovered the beam contamination issues affecting the O’Neil et al. (2000a) Arecibo 305m single-dish results. The maps for P1-2, P1-3 and C6-1 show clearly that the H I is all at the position of neighboring spiral galaxies. The H I detection for C4-2 was confirmed, but the map of C4-1 did not detect any H I even though the VLA observations were sufficiently deep to detect the H I, if it were present at the level measured at Arecibo. This result suggests that the N9-2 and C1-2 H I detections may also be noise artifacts, and not starless gas clouds.

We compare our emission line strength measurements for the post-starburst dwarf galaxy NGC 1569 with the results of Kobulnicky & Skillman (1997). Our aperture lies perpendicular to the C and D slit placements of their work and near the two super-star clusters. Kobulnicky & Skillman found that the combination of galactic and intrinsic reddening is both large and variable over the face of this galaxy. In accordance with their methods, we choose a value for the total extinction (galactic plus intrinsic) which brings our measured $H\alpha/H\beta$ ratio to 2.83 after applying the reddening correction. We measure a total $E(B-V)$ of 0.83, which is within the range of values found by Kobulnicky & Skillman (following Kobulnicky & Skillman and Burstein & Heiles (1982), we assume that 0.5 mag of the reddening originates in our galaxy). Once we apply the extinction correction to all the emission lines, our relative flux measurements for the lines $H\gamma$ (0.45 ± 0.01), $[O\ III]\lambda\lambda 4959,5007$ (1.94 ± 0.01 , 5.72 ± 0.01 , respectively), $[S\ III]\lambda 6312$ (0.008 ± 0.001), $[N\ II]\lambda\lambda 6548,6584$ (0.042 ± 0.001 , 0.098 ± 0.001 , respectively), $HeI\lambda 6678$ (0.023 ± 0.001), and $[S\ II]\lambda\lambda 6717,6731$ (0.137 ± 0.002 , 0.100 ± 0.001 , respectively) all lie within the range covered by the Kobulnicky & Skillman measurements for this part of the galaxy. The only discrepant line is $[O\ III]\lambda 4363$ (0.124 ± 0.007), which lies on the blue end of our spectrum where the flux calibration is less secure. Over the wavelength range 4800 Å to 7000 Å, our emission line measurements are fully consistent with the results of Kobulnicky & Skillman.

The absorption line index strengths for NGC 3872 are compared with the results of Trager et al. (1998). We extract the spectra using a spatial aperture equivalent to the Lick/IDS aperture, and make velocity dispersion corrections appropriate for $\sigma_{NGC3872} = 250$ km/s. Trager et al. (1998) measure the following values: $H\beta$: 1.28 ± 0.22 ; Mgb : 4.91 ± 0.30 ; $\langle Fe \rangle$: 2.22 ± 0.22 . Our measurements for $H\beta$ and Mgb are within 1σ of their values. For $\langle Fe \rangle$, our measurement is about 2.5σ higher than theirs.

3. PRESENTATION OF THE SPECTRA

We present the spectra in Figures 3a-e and 4. The spectra for these 19 LSB galaxies qualitatively resemble the spectra of HSB galaxies over the full range of spectra seen for all Hubble types, from ellipticals all the way through late-type spirals and starbursting irregular galax-

ies. For comparison, we show our spectra of the two elliptical galaxies, NGC 3872 and UGC 3844, in Figure 3a, and the spectrum of the post-starburst irregular galaxy NGC 1569 in Figure 3d.

The emission line galaxies have been ordered by the strength of their $[N\ II]\lambda 6584$ emission relative to $H\alpha$, from strongest to weakest. This is essentially a sequence of decreasing metallicity as we will show in Section 6. The strength of the $[O\ III]\lambda 5007$ emission line increases along the sequence, due to a combination of the decreasing metallicity and the associated decreasing amount of dust reddening in the emission regions. This will be discussed in Section 7.

The spectral extraction was done using global apertures, which blend together stellar light and line emission from both H II regions and diffuse emission regions. While we do not generally have sufficient spatial resolution to observe gradients in the galaxy properties, we note that the galaxy U1-4 has a clear inner and outer region. The inner region of radius $3''$ is dominated by a bright continuum with stellar absorption features. Outside this region there is a peak in the emission on both sides of the nucleus at about $5''$. Further out, both the emission and continuum fall off. This is illustrated in Figure 5. The spectroscopic aperture we use for this galaxy is $2'' \times 32''$ and includes light from both the inner and outer regions.

Analysis of the galaxies in Figure 3(a-d) will be presented in the following sections. Here we discuss in detail the galaxies presented in Figures 3e and 4.

The galaxy N9-2 (Figure 4) has a redshift of 0.246 ($cz=73629$ km s^{-1}). The restframe wavelength coverage for this galaxy is significantly bluer than the rest of the sample, and we do not have observations of the wavelength region near $H\alpha$. After applying the $(1+z)^4$ cosmological surface brightness correction and a k_B correction appropriate for an Scd galaxy near $z=0.2$ of 0.45 mag (Frei & Gunn 1994), N9-2 has $\mu_B(0) = 22.1$ well within the range of high surface brightness galaxies. N9-2 is just a normal HSB spiral galaxy, seen at moderate redshift, and so we remove it from the rest of the analysis.

The galaxies N10-4 and C5-5 (Figure 3e) both have $\mu_B(0) = 24$ and are among the faintest in our sample. The S/N of the observations are sufficient to determine redshifts for these two galaxies, but insufficient for a more detailed analysis. N10-4 is particularly interesting, however, because of its companions. There were two other objects which serendipitously fell onto the slit during the observations. We refer to these as N10-4a and N10-4b. N10-4a ($11^h58^m52^s.5$, $20^\circ58'23''$ J2000) lies $4h^{-1}$ kpc away ($12''$) from the center of N10-4. We detect emission lines of $H\alpha$, $H\beta$, and $[O\ III]\lambda\lambda 4959,5007$ in the companion, shifted 65 km s^{-1} blueward ($cz_{hel}=7382$ km s^{-1}). We do not detect anything in the broadband setup image at this position, making it difficult to determine whether this is a separate system, or a knot of emission in the outer disk of N10-4. Additionally, there is another companion $16''.5$ in the opposite direction along the slit (N10-4b, $11^h58^m50^s.8$, $20^\circ58'33''.5$ J2000). This object is also not seen in the setup image, or in images from the digitized sky survey. We do not detect any continuum from this object and only one emission line is seen. This line is detected in all four observations of N10-4. The spectrum is presented in Fig-

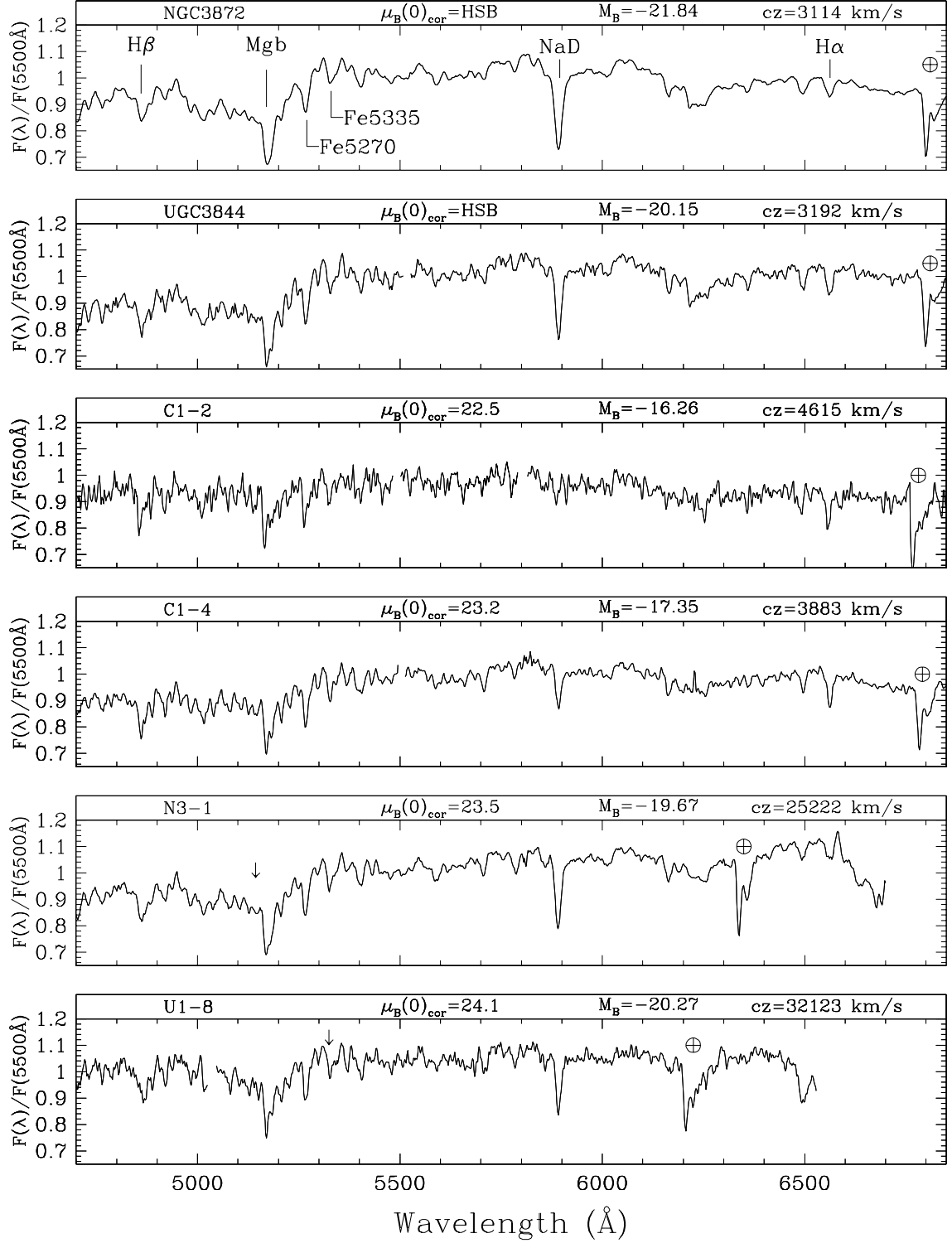


FIG. 3A.— Presentation of spectra for galaxies at low redshift ($z < 0.11$). The strongest absorption features are labelled in (a), and the strongest emission lines are labelled in (c). (a) Objects with absorption dominated spectra. The top two galaxies are bright ellipticals for comparison purposes, while the bottom four spectra are LSB galaxies. Gaps in the data mark regions affected by large sky subtraction residuals. The location of the atmospheric B band absorption ($\simeq 6840 \text{ \AA}$ in the observed frame) is marked with \oplus . Vertical arrows denote the regions affected by sky subtraction residuals which were corrected via interpolation using the V1999 stellar population model spectra (see Section 2.3.6). Note that with the high S/N of the observations for NGC 3872, C1-4, and N3-1, the majority of the bumps and wiggles are real features, and not noise.

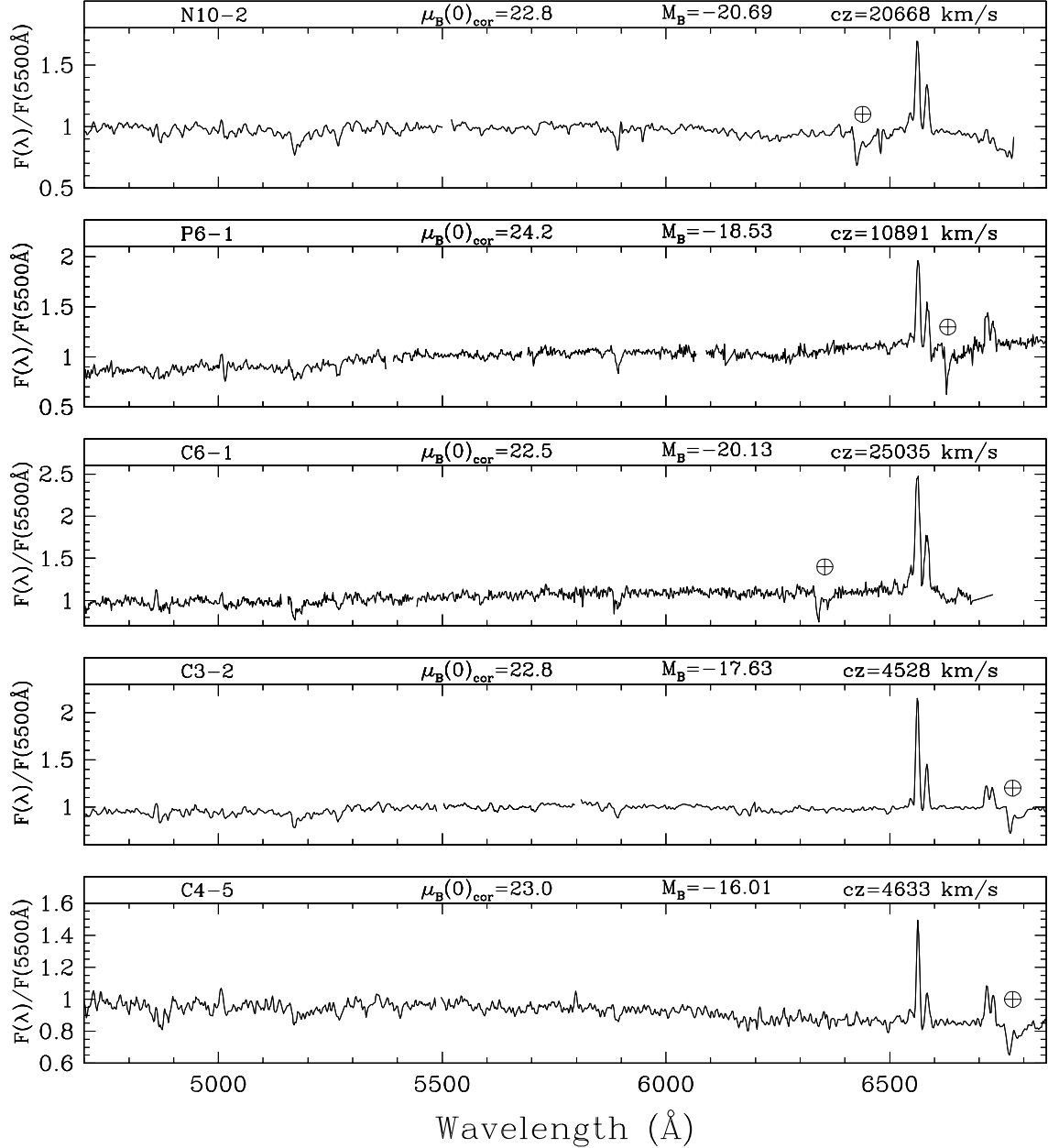


FIG. 3B.— Spectra for LSB galaxies with emission lines, ordered by the strength of $[\text{N II}]\lambda 6584$ relative to $\text{H}\alpha$.

ure 4. The observed wavelength of this emission line is 5738.9 \AA , which translates to 5600 \AA in the restframe of N10-4. This wavelength does not match any commonly observed galaxy emission lines. Instead, we suggest that this object is a background galaxy, and the single line observed at 5738.9 \AA corresponds to $[\text{O II}]\lambda 3727$ seen at a redshift of 0.54. At this redshift, our restframe wavelength coverage is 2790 \AA to 4700 \AA , where we do not expect to see any other strong emission lines.

The SED of C5-5 (Figure 3e) has a bump in it, centered at 5600 \AA (5670 \AA in the observed frame) which we do not have an explanation for. The bright spiral galaxy UGC

4416 fills the edge of the slit, and some of its light might be scattering in. There is also a spatial offset between the emission line peak and the peak of the continuum for this galaxy, though the emission is still consistent with coming from C5-5. Due to the low S/N of these observations, we do not include either N10-4 or C5-5 in the remainder of the analysis.

4. EMISSION LINE SOURCE: H II REGIONS VS. AGN

We use the diagnostic diagrams of Veilleux & Osterbrock (1987) to determine whether the emission lines in the observed LSB galaxies come from active galactic nuclei (AGN) or H II regions. Figure 6a shows the

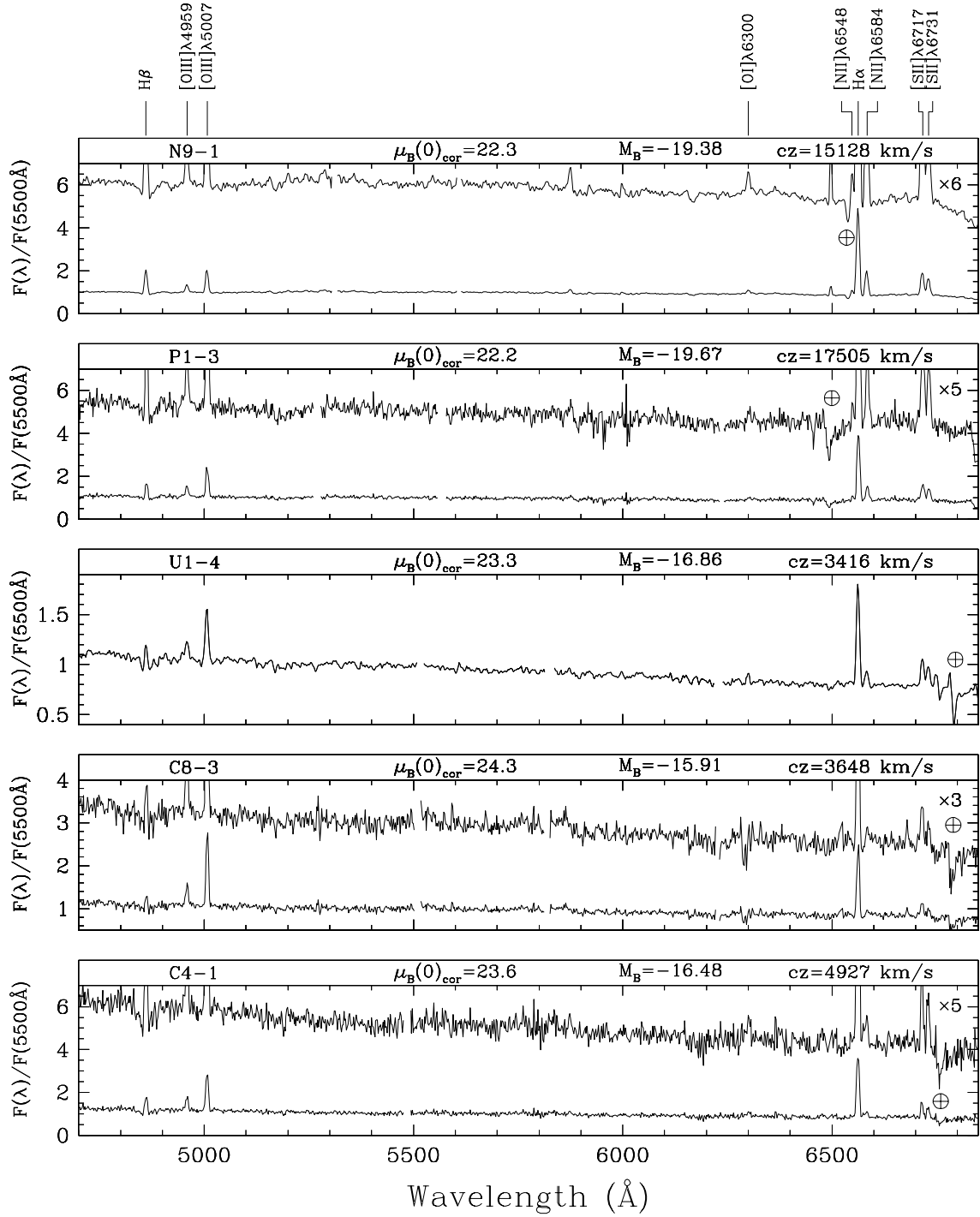


FIG. 3c.— Spectra for LSB galaxies with emission lines, ordered by the strength of $[\text{N II}]\lambda 6584$ relative to $\text{H}\alpha$.

$[\text{N II}]\lambda 6584/\text{H}\alpha$ vs. $[\text{O III}]\lambda 5007/\text{H}\beta$ diagnostic. We overplot the theoretical separation line of Kewley et al. (2001a) on the diagram. The LSB galaxies all clearly lie in the H II

side of the diagram. They also lie in the same area of the diagram as the HSB galaxies from the Nearby Field Galaxy Survey (NFGS; Jansen et al. 2000). Figure 6b shows the

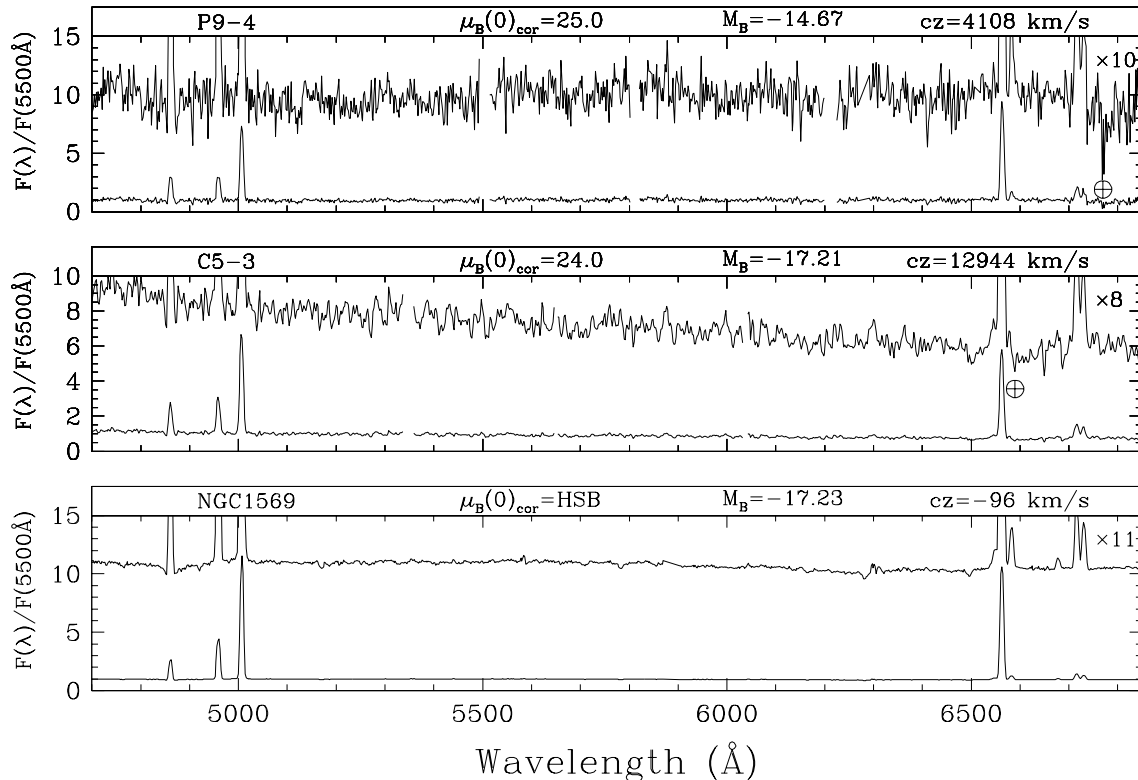


FIG. 3D.— Spectra for galaxies with very weak $[\text{N II}]\lambda 6584$ and large $\text{EW}(\text{H}\alpha)$. NGC 1569 is a high surface brightness post-starburst galaxy.

$[\text{S II}]\lambda 6717 + \lambda 6731 / \text{H}\alpha$ vs. $[\text{O III}]\lambda 5007 / \text{H}\beta$ emission line diagnostic. The interpretation here is less clear. The LSB galaxies all lie on the separatrix, and there is considerably more scatter amongst the NFGS galaxies as well. Kewley et al. (2001b) note that the $[\text{S II}]\lambda 6717 + \lambda 6731 / \text{H}\alpha$ ratio is sensitive to the local density, and therefore might be a less reliable diagnostic than the $[\text{N II}]\lambda 6584 / \text{H}\alpha$ ratio. N10-2 shifts dramatically between the two diagnostics, relative to the rest of the LSB galaxies. This is an instrumental effect, as the redshifted $[\text{S II}]$ lines fall just at the red end of our spectral coverage, where the flux calibration is less secure. All the galaxies with emission lines are consistent with star formation as the ionizing source, rather than AGN.

5. MEAN AGE AND METALLICITY OF THE STARS

The degeneracy between the effects of age and metallicity on broadband optical colors and individual spectral features has been well documented (O’Connell 1976; Worthey 1994; Rose 1994). This degeneracy can be broken by using combinations of two or more absorption features, with different sensitivity to age and metallicity (Worthey et al. 1994; Jørgensen 1997; Vazdekis 1999; Kuntschner et al. 2001). We use the line index $\text{H}\beta$ which is more age sensitive, in conjunction with the more metal sensitive indices Mgb and $\langle \text{Fe} \rangle$. In Figure 7 we plot grids of age and metallicity for single stellar populations derived from the V2000 models, on the axes of $\text{H}\beta$ vs. Mgb and $\text{H}\beta$ vs. $\langle \text{Fe} \rangle$. Within this grid, we determine the mean luminos-

ity weighted age and metallicity for the stellar populations of the four absorption line dominated LSB galaxies, C1-2, C1-4, N3-1, and U1-8. We also plot the two elliptical galaxies which we observed, as well as the locus of points covered by the Coma cluster elliptical and S0 galaxies from Jørgensen (1999).

The three LSB galaxies C1-2, C1-4 and U1-8 all lie together on the plots, in the low metallicity regime. They all have mean ages around 5.5 Gyr. C1-4 has near solar metallicity, while C1-2 and U1-8 have about half solar metallicity.

In contrast, N3-1 has a much higher metallicity, appearing at 1.5 times solar metallicity in the $\text{H}\beta$ vs. $\langle \text{Fe} \rangle$ plot, and even higher in the $\text{H}\beta$ vs. Mgb plot. This is the regime shared by luminous elliptical and S0 galaxies. Furthermore, note how N3-1 as well as the elliptical and S0 galaxies shift with respect to the model grid between the two plots. This is the signature of super-solar $[\text{Mg}/\text{Fe}]$ abundance ratios. This enhancement effect is well known for luminous galaxies, both spirals and ellipticals, and the strength of the enhancement is correlated with galaxy mass and velocity dispersion (Worthey 1998; Jørgensen 1999; Kuntschner et al. 2001). The other three LSB galaxies do not move relative to the model grid between the two plots; these galaxies all have solar $[\text{Mg}/\text{Fe}]$ abundance ratios.

Figure 8 more clearly illustrates the $[\text{Mg}/\text{Fe}]$ issue. This plot shows the $\langle \text{Fe} \rangle$ index plotted against the Mgb index. Since these two indices have similar metallicity and

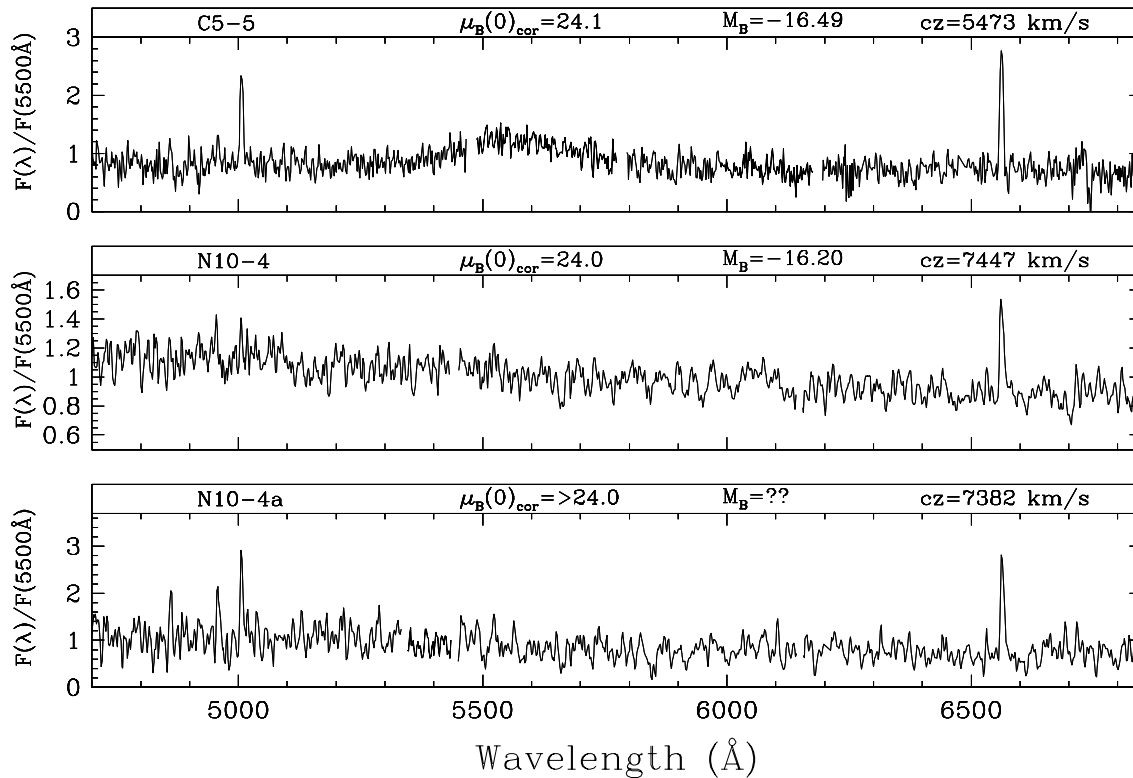


FIG. 3E.— The S/N of the spectra for N10-4 and C5-5 are too low to estimate the galaxies’ metallicities, but the spectra are suitable for determining redshifts. See the text for a description of N10-4a.

age sensitivity, the model grid for differing ages and metallicities is not well separated in this plane. Galaxies with solar $[\text{Mg}/\text{Fe}]$ should fall onto the narrow region covered by the model grid, as indeed most of the LSB galaxies do. On this Figure we also show the LSB galaxies with emission lines which have reliable Mgb and $\langle \text{Fe} \rangle$ measurements. The bulk of the elliptical and S0 galaxies as well as N3-1 fall to the right of the model grid, a failure of the models to account for the $[\text{Mg}/\text{Fe}]$ appropriate to these galaxies.

There is another caveat with these models, especially important when dealing with low metallicity stellar populations. These models do not include blue horizontal branch or post-AGB stars, which will have an effect on measured Balmer line strengths (Maraston & Thomas 2000). However, at the lowest metallicities found here (a tenth solar to a fifth solar), galactic globular clusters do not show a blue horizontal branch, and thus we do not expect contamination by these blue stars to be a significant effect. Furthermore, the effect of these stars on integrated spectra is to increase the strength of the $\text{H}\beta$ absorption, leading to younger apparent ages. The main conclusion of this section is that some LSB galaxies do in fact have old mean ages; a correction for these blue stars would only strengthen our conclusion.

6. GAS PHASE METALLICITY AND AGE INDICATORS

Much as we used the stellar absorption indices to study the older stellar populations, we would like to use emission

line strengths and ratios to characterize the metallicity of the gas and the properties of the young stellar populations. The equivalent width of $\text{H}\alpha$, $\text{EW}(\text{H}\alpha)$, compares the flux from hot young stars, capable of ionizing nebulae, to the red flux from the stellar population, which is dominated by long-lived lower mass stars for a standard (e.g. Salpeter 1955) initial mass function (IMF). Consequently, the $\text{EW}(\text{H}\alpha)$ can be used as a mean age indicator for the integrated stellar population. The conversion between $\text{EW}(\text{H}\alpha)$ and the Scalo (1986) birthrate parameter, defined as $b \equiv \frac{\text{SFR}}{\langle \text{SFR} \rangle_{\text{past}}}$, is sensitive to both the form of the star formation history (SFH) and the IMF, and hence is quite model dependant. A single burst of star formation will only produce $\text{H}\alpha$ emission for ~ 30 Myr after which the massive stars ($M_* > 15 M_\odot$) which produce the ionizing flux have all died off. Models with continuous star formation and multiple burst models that produce an underlying old population plus a new burst will both produce $\text{H}\alpha$ emission at later times. Kennicutt, Tamblyn, & Congdon (1994) use stellar population and nebular models to derive a relation between $\text{EW}(\text{H}\alpha)$ and b appropriate for galaxies with a constant or exponentially decreasing SFR. The relation they derive, based on a Salpeter (1955) IMF with upper and lower mass limits of 100 and $0.1 M_\odot$, a 10 Gyr age and varying exponential decay times, shows a monotonic increase of b with $\text{EW}(\text{H}\alpha)$, and has $b=1$ at $\text{EW}(\text{H}\alpha)=64 \text{ \AA}$. van den Hoek et al. (2000) found that chemo-evolutionary models with an exponentially de-

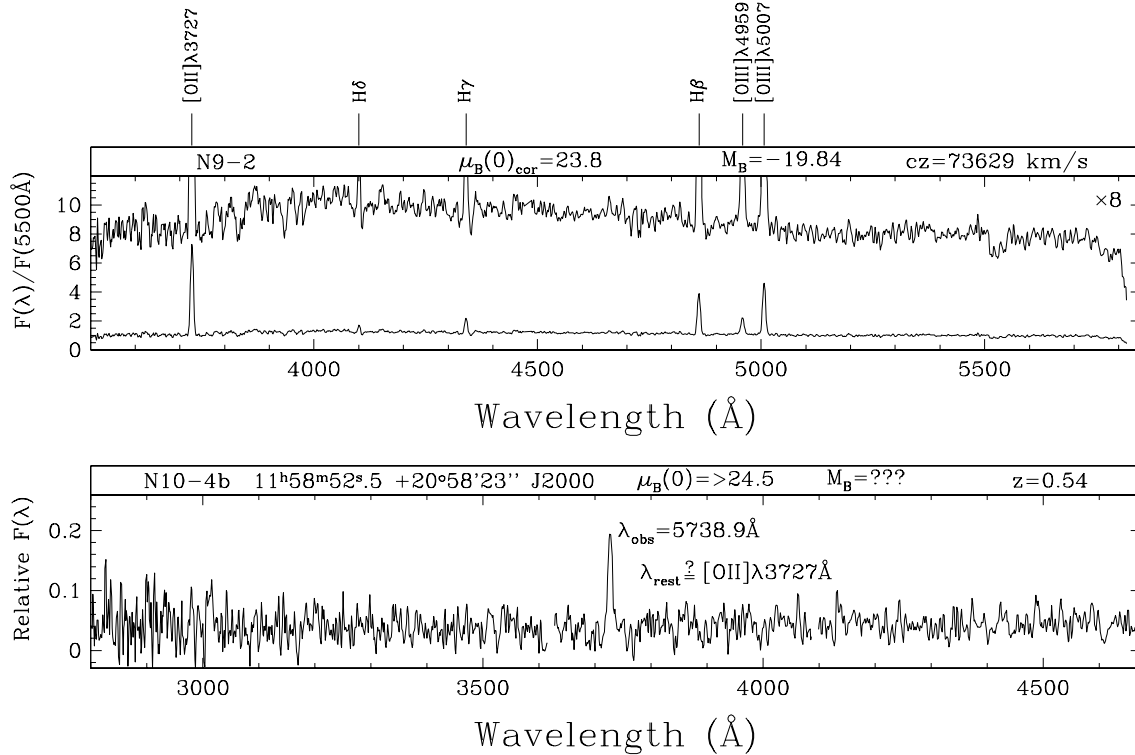


FIG. 4.— Spectra for galaxies with $z > 0.2$: a) N9-2 is at $z \simeq 0.245$, and is most likely a normal high surface brightness spiral galaxy affected by cosmological surface brightness dimming. b) N10-4b is detected as a single emission line at $\lambda = 5738.9 \text{ \AA}$, which we identify as $[\text{O II}]\lambda 3727$ emission at $z=0.54$. No object is seen in the broadband imaging with the HET or PFC at the location of this object, suggesting it could be a high redshift LSB galaxy.

creasing SFR were sufficient to describe the LSB galaxies in their sample with $(B-V) > 0.4$ but that additional star formation bursts were needed to explain bluer galaxies. The measured $\text{EW}(\text{H}\alpha)$ for an old-plus-burst stellar population will of course depend on both the age of the burst, and the stellar mass fraction that it embodies. In Figures 10 and 12 we show the b calibration of Kennicutt et al. (1994) on the right vertical axis, but give the caveat that this calibration is inappropriate for an old-plus-burst SFH.

Traditional methods of studying gas phase chemical abundances in H II regions require measurements of several H or He recombination lines, along with collisionally excited lines from multiple ionization states of a heavier metallic species. Osterbrock (1989) details the method for studying individual H II regions. Kobulnicky et al. (1999) extend this work and look at the effect on the derived abundances of smearing together the light from multiple H II regions in a single galaxy into a single spectroscopic aperture, using abundance analysis methods such as the semi-empirical strong-line R_{23} method (Pagel et al. 1979; Osterbrock 1989; McGaugh 1991, 1994). The wavelength range covered by our spectra rarely includes the $[\text{O II}]\lambda 3727 \text{ \AA}$ line used in the R_{23} method. Instead, we choose to use the metallicity indicator $[\text{N II}]\lambda 6584/\text{H}\alpha$ (hereafter $[\text{N II}]/\text{H}\alpha$) proposed by Storchi-Bergmann, Calzetti, & Kinney (1994). This measurement has the advantage of being monotonic (as op-

⁴ $\log(R_{23}) = \log\left(\frac{[\text{O II}]\lambda 3727 + [\text{O III}]\lambda \lambda 4959, 5007}{\text{H}\beta}\right)$

posed to the double valued nature of the R_{23} method) and is essentially reddening independent by virtue of the small wavelength split between the two lines. Empirical calibrations between $[\text{N II}]/\text{H}\alpha$ and $\log(\text{O}/\text{H})$ (determined using the R_{23} method) have been derived from observations of individual H II regions (e.g. van Zee et al. 1998) and for galaxies (Denicoló, Terlevich, & Terlevich 2002). The drawback to using $[\text{N II}]/\text{H}\alpha$ is that this ratio is sensitive to the ionization state, which will vary between H II regions and the diffuse ISM, and is difficult to determine for globally averaged spectra. Kewley & Dopita (2002) provide a theoretical calibration of $[\text{N II}]/\text{H}\alpha$ vs. metallicity for starburst galaxies, including the effects of the ionization parameter. McGaugh (1994) find for H II regions in LSB galaxies that the ionization parameter $\log\langle U \rangle$ varies between -2 and -3.5 , while Denicoló et al. find that $\log\langle U \rangle = -2.0$ is most representative for their sample of galaxies. However, a change in $\log\langle U \rangle$ of $+0.5$ dex or -1.0 dex leads to an uncertainty in the metallicity zero-point of ± 0.3 dex. There was no correlation seen between metallicity and $\log\langle U \rangle$ in the McGaugh dataset. In the plots that follow, we label one axis with the Denicoló et al. empirical calibration of $[\text{N II}]/\text{H}\alpha$, but we give the caveat that the zero-point of this calibration may be high by $\simeq 0.3$ dex and that any systematic changes of the ionization parameter with other parameters of these galaxies such as age may lead to a misinterpretation of the $[\text{N II}]/\text{H}\alpha$ ranking as a strict metallicity scale.

We compare the gas phase metallicity indicator $[\text{N II}]/\text{H}\alpha$

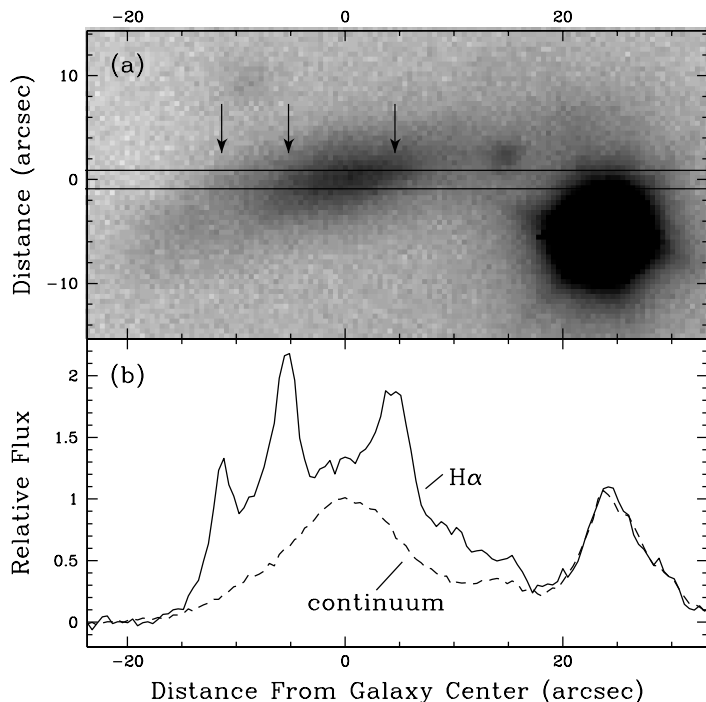


FIG. 5.— The galaxy U1-4: (a) image of U1-4 taken with the HET during set-up for the spectroscopic observation. The object at the lower right is a bright star. The three arrows correspond to the regions of the slit where emission peaks are seen. (b) spatial cut across the 2D spectrum. Solid line - flux of the $H\alpha$ line (average over $6569.0\text{\AA} - 6565.9\text{\AA}$ in the U1-4 restframe); Dashed line - continuum flux blueward of $H\alpha$ (average over $6495.3\text{\AA} - 6540.8\text{\AA}$ in the U1-4 restframe). The $H\alpha$ emission is more spatially extended than the stellar continuum light, and three peaks are seen in the emission (spatial) profile, at $-12''$, $-5''$ and $+5''$ from the galaxy center. We don't see the emission regions in (a), which is a broadband image. The spatial profile of the star in (b) shows the image PSF for this observation (the wavelength regions in the restframe of the star are $6633.7\text{\AA} - 6640.7\text{\AA}$ and $6569.3\text{\AA} - 6615\text{\AA}$).

with the stellar absorption indices Mgb and $\langle Fe \rangle$ in Figure 9. There are clear correlations with each index. A Kendall's τ test gives a probability of 1.6% that $[N II]/H\alpha$ and Mgb are not correlated, and a probability of 0.08% that $[N II]/H\alpha$ and $\langle Fe \rangle$ are not correlated. The best fit fits are:

$$[NII]/H\alpha = -0.11(\pm 0.13) + 0.26(\pm 0.08) \cdot \langle Fe \rangle \quad (1)$$

$$[NII]/H\alpha = -0.01(\pm 0.09) + 0.16(\pm 0.05) \cdot Mgb \quad (2)$$

It is perhaps surprising that the correlations are so strong, given the age-metallicity degeneracy of the stellar indices and the variation of the $[N II]/H\alpha$ calibration with ionization parameter. Panels c and d in Figure 9 show the age indicator $EW(H\alpha)$ plotted against the absorption line indices. At low Mgb strength, we see a wide range of $EW(H\alpha)$ strengths, which diminishes at higher Mgb strengths. In models with continuous, exponentially decreasing SFR, the metallicity increases as the gas fraction decreases. Simultaneously, the SFR drops and the fractional galaxy mass made up by low mass stars increases. This will result in a decrease of $EW(H\alpha)$ and simultaneous increase of Mgb over time, leading to an upper envelope in the $EW(H\alpha)$ vs Mgb plane, much as we see here. For “open box” chemical evolution models (models in which

enriched gas is allowed to escape due to stellar winds and supernovae), the low $EW(H\alpha)$ and low Mgb region will get filled in by galaxies with low total mass, where the star formation rate drops once the gas is expelled, and before metallicity builds up. In any case, once star formation stops completely, the $EW(H\alpha)$ will drop to zero, and the Mgb index will slowly strengthen as the stellar population ages (at constant metallicity). This picture holds equally well for the $\langle Fe \rangle$ strength as for Mgb . A quantitative analysis of where models with continuous star formation would lie on the $EW(H\alpha)$ vs. metal absorption index plots requires models that contain both nebular emission spectra, and stellar absorption line strengths. Unfortunately, there are not yet any such models in the literature. Within the picture of continuous star formation, we can also give a qualitative explanation for the strong correlation seen between $[N II]/H\alpha$ and Mgb or $\langle Fe \rangle$. $[N II]/H\alpha$ reflects the current metallicity of the gas. The ionization parameter is a small source of scatter, but is not (apparently) significant. The Mgb and $\langle Fe \rangle$ strengths are responsive to both the metallicity and age of the stellar population, but since these are linked by the gas consumption and enrichment history, a correlation exists between the current metallicity and the age and enrichment history of the stellar population.

An alternative explanation can be given by a model with an old stellar population underlying a young burst of star formation. In this case, the mass fraction of the burst and metallicity of the old population will determine the evolutionary track of a galaxy through the $EW(H\alpha)$ vs. Mgb (or $\langle Fe \rangle$) plane. The mass fraction determines how much blue continuum light from the young stellar population there will be to veil the strength of the underlying metal line absorption. The $H\alpha$ flux is driven by very short-lived stars, while the continuum veiling effect evolves over longer timescales ($\simeq 0.5$ Gyr vs. $\simeq 30$ Myr for the $H\alpha$). Consequently, the tracks will move vertically down the diagram, and then to the right at late times. The track will end at the absorption line strength of the underlying population for small bursts, and the offset between where the track descends vertically and where it ends depends on the mass fraction of the burst. To illustrate this, we use the Starburst99 models (Leitherer et al. 1999) for the evolution of an instantaneous burst population, along with the V2000 stellar population models for the underlying population. In Figure 9(c-d) we plot the data for the LSB galaxies together with model tracks for galaxies with a 5 Gyr old, solar metallicity underlying population, and a 10%, 2%, 1%, and 0.1% (by mass) instantaneous burst. It is clear that by varying the age and metallicity of the underlying population, or by varying the burst mass fraction, it is possible to fill in every part of the plot. While we do not find LSB galaxies in all parts of the plot, we have a small sample and do not strongly constrain against the possibility of galaxies in the high $EW(H\alpha)$ and high Mgb (or $\langle Fe \rangle$) region of the diagrams.

It is possible to fully explain the $EW(H\alpha)$, Mgb , and $\langle Fe \rangle$ data with an old (> 5 Gyr) solar metallicity population and varying burst mass fractions. However, with this model the $[N II]/H\alpha$ vs. Mgb correlation becomes difficult to explain. The $[N II]/H\alpha$ value should reflect the metallicity of the burst, which is presumably greater than

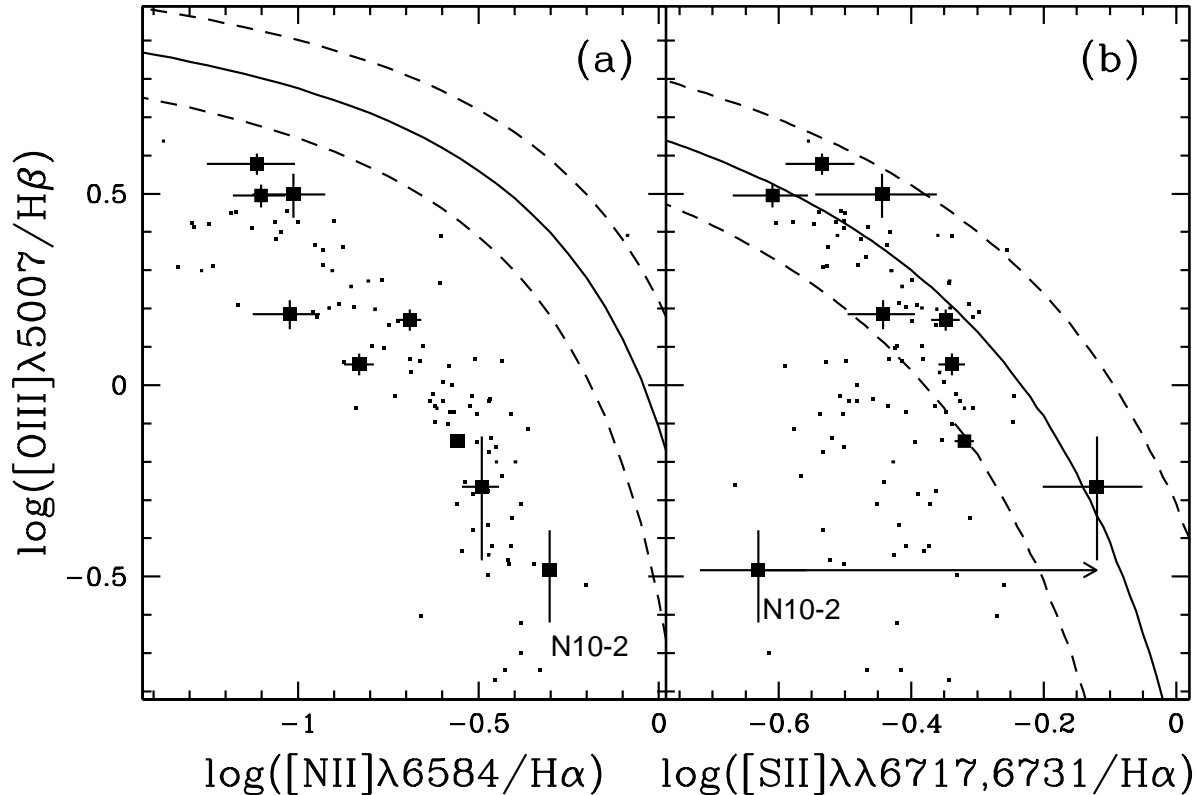


FIG. 6.— Ionization diagnostic diagrams: large boxes – LSB galaxies; small boxes – galaxies in the NFGS sample (Jansen et al. 2000); lines – theoretical classification line and ± 0.1 dex error range separating AGN from starburst (H II) galaxies, from Kewley et al. (2001a). The LSB galaxies are all well within the H II region for the $[\text{N II}]/\text{H}\alpha$ vs $[\text{O III}]/\text{H}\beta$ diagnostic. There is a shift in the data with respect to the theoretical separatrix in the $[\text{S II}]/\text{H}\alpha$ vs $[\text{O III}]/\text{H}\beta$ diagnostic. However, the LSB galaxies are all still consistent with starburst like spectra. The shift of N10-2 between (a) and (b) is a result of poor flux calibration at the extreme red end of the spectrum, which affects the $[\text{S II}]/\text{H}\alpha$ measurements. The arrow shows the uncertainty in $[\text{S II}]/\text{H}\alpha$ for N10-2 due to this systematic effect.

or equal to the metallicity of the underlying stellar population. If the underlying stellar population is always metal rich and the burst mass fractions were random, pushing the absorption line indices to lower levels, there would not be a correlation between $[\text{N II}]/\text{H}\alpha$ and the absorption indices. Consequently, it appears that old-plus-burst models are only viable if the old populations have a range of metallicities, and if any one burst constitutes only a small fraction of the stellar mass (less than $\sim 0.3\%$) such that the absorption indices are not perturbed from that of the underlying population.

Our understanding of these correlations is hampered by the small size of our sample, and discontinuity between models which predict nebular emission strengths from young stellar populations, and models which predict the stellar metal absorption line indices for older, cooler populations. Ideally, we could glean a better understanding of these correlations from a larger sample of LSB or HSB galaxies. However, we have been unable to find published studies of HSB galaxies which include data on both the stellar absorption indices and emission line strengths. The NFGS and Sloan Digital Sky Survey (though the latter is prone to aperture effects) represent two datasets upon which it would be enlightening to make this study.

We cannot measure gas phase abundances for the four absorption line dominated galaxies, but we use the correla-

tions in Equations (1) and (2) to assign values of $[\text{N II}]/\text{H}\alpha$ to these galaxies. We do this primarily so that we can include these four galaxies on the remainder of the diagnostic diagrams, where we use $[\text{N II}]/\text{H}\alpha$ as a metallicity indicator. We interpolate the relations get values for C1-2 and U1-8, and extrapolate to get values for C1-4 and N3-1. The values determined from each of the two correlations are averaged, to reduce the uncertainties. The assigned $[\text{N II}]/\text{H}\alpha$ values are as follows: 0.47 ± 0.15 for C1-2; 0.47 ± 0.14 for U1-8; 0.55 ± 0.16 for C1-4; 0.71 ± 0.19 for N3-1. These four galaxies are shown as open circles on Figure 9. The absorption line dominated galaxies seem to lie at one end of a continuous sequence of spectral properties, as illustrated by Figs. 3a - 3d. This suggests that the extrapolation of these correlations is reasonable. However, we do note that stellar populations at constant metallicity will evolve to higher Mgb and $\langle \text{Fe} \rangle$ with age once the star formation stops. Though we do not see a large age spread among the four absorption dominated systems, age will affect the extrapolation of these relations to higher index strengths. By including both the absorption and emission line galaxies in Figures 10 and 12 we attempt to show these galaxies potentially have very similar evolutionary histories (though they are perhaps at different stages of that evolution). The emission associated with a small burst of star formation is very short-lived, and though the

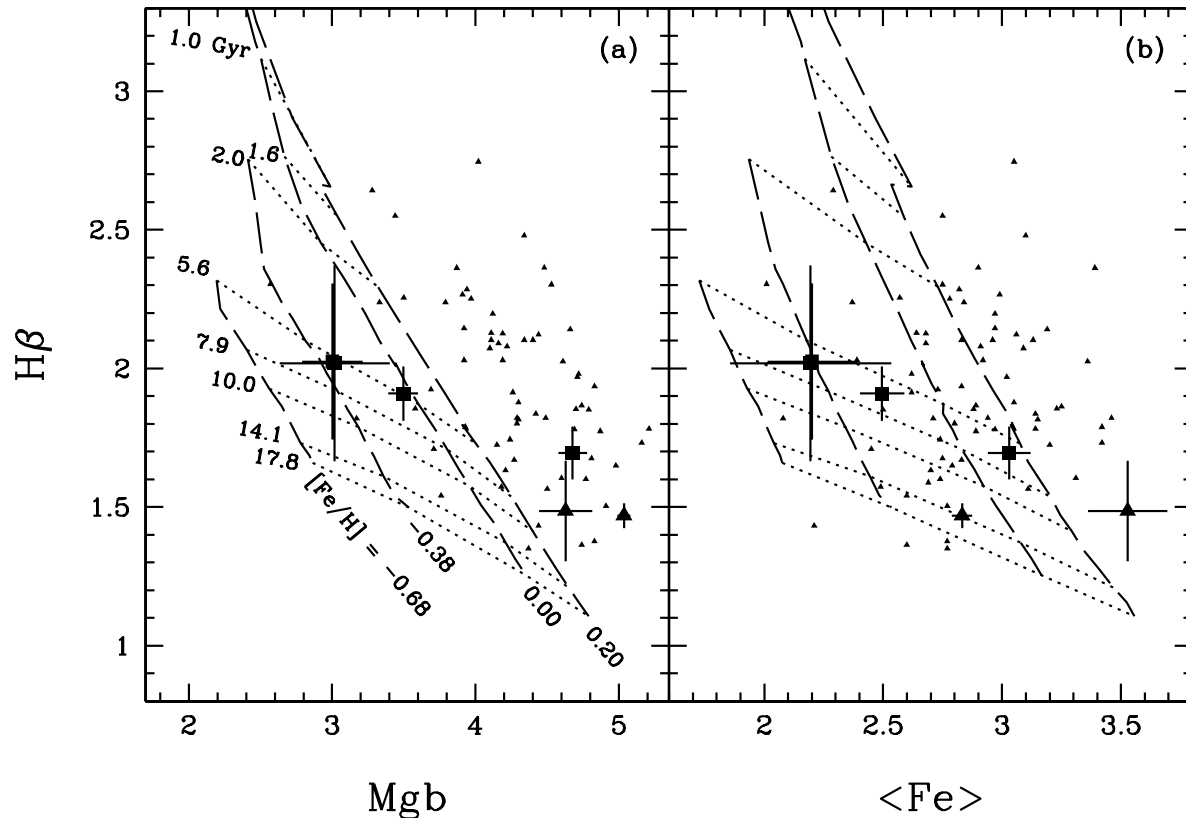


FIG. 7.— $H\beta$ absorption line index vs. the Mgb index (left) and the $\langle Fe \rangle$ index (right). Boxes: LSB galaxies; Large triangles: our data of HSB ellipticals; small triangles: Coma cluster elliptical and S0 galaxies from Jørgensen (1999). The model grid shows lines of constant age (dotted) and constant metallicity (long dash), from V2000 as labelled. The same age and metallicity values are used for the grid in both panels. The four LSB galaxies plotted are (in order of increasing Mgb, $\langle Fe \rangle$ strength) U1-8, C1-2, C1-4, and N3-1. Note that the points for C1-2 and U1-8 lie virtually on top of each other. The Coma cluster galaxies, N3-1, and NGC 3872, shift relative to the model grid in the two plots. This is caused by the well known super-solar $[Mg/Fe]$ ratio in luminous elliptical and S0 galaxies, which is not reproduced by the models.

emission line flux can be significant, the associated effect on the chemical evolution and continuum luminosity could be slight, and so understanding these two "classes" of LSB galaxies, absorption and emission line galaxies, is necessarily intertwined.

In Figure 10 we plot $[N II]/H\alpha$ against the $EW(H\alpha)$ for the LSB galaxies. The metallicity and birthrate calibrations discussed at the beginning of this section are included on the axes opposing the measured parameters. We also plot the HSB galaxies from the NFGS (Jansen et al. 2000), which satisfy the condition that $EW(H\alpha) > 9 \text{ \AA}$ (i.e. those which have a small measurement uncertainty for the $[N II]/H\alpha$ line ratio). The LSB galaxies fill the same region of the $[N II]/H\alpha$ vs. $EW(H\alpha)$ parameter space, suggesting a similar star formation and chemical enrichment history to that of HSB galaxies. At low metallicities there is a wide range of mean ages, however the relative current SFR decreases as metallicity increases. This makes sense for continuous star formation, as the bulk of the gas in these galaxies must have been previously processed into stars to raise the mean metallicity, and consequently there is less gas around to make new stars.

7. DUST CONTENT

The amount of internal reddening in LSB galaxies is not well known, but of great importance to attempts at

modelling their formation and evolution. In Figure 11a we plot the Balmer ratio, $H\alpha/H\beta$, versus the metallicity indicator $[N II]/H\alpha$. The Balmer ratio can be used to derive the internal reddening of the emission line regions. Using the Cardelli extinction law (Cardelli et al. 1989), with $R_V = 3.1$, we derive the following relation:

$$E(B - I_c) = 2.375 \cdot E(B - V) = \frac{\log\left(\frac{f(H\alpha)}{f(H\beta)}\right)}{0.172} - 2.65 \quad (3)$$

This relation is used to place an $E(B - I_c)$ scale on the right axis of Fig. 11. We use the NFGS (Jansen et al. 2000) as a comparison sample of HSB emission line galaxies. The NFGS galaxies were not observed in the I-band. We convert their $(B - R_c)$ colors to $(B - I_c)$ colors using the relation $(B - I_c) = 1.34 \cdot (B - R_c) + 0.18$, derived from the mean galaxy colors of Fukugita, Shimasaku, & Ichikawa (1995). Central surface brightnesses were not derived for the NFGS galaxies. In the LSB data, we have not corrected the measured $H\alpha$ fluxes and equivalent widths for underlying stellar absorption. This correction will move points upwards and to the left in the $H\alpha/H\beta$ vs. $[N II]/H\alpha$ plane. While the uncorrected data show a trend for LSB galaxies to have lower extinction than HSB galaxies at the same metallicity, an $H\alpha$ equivalent width correction of 1.5 \AA would move most of the LSB galaxies onto the locus of HSB galaxy points.

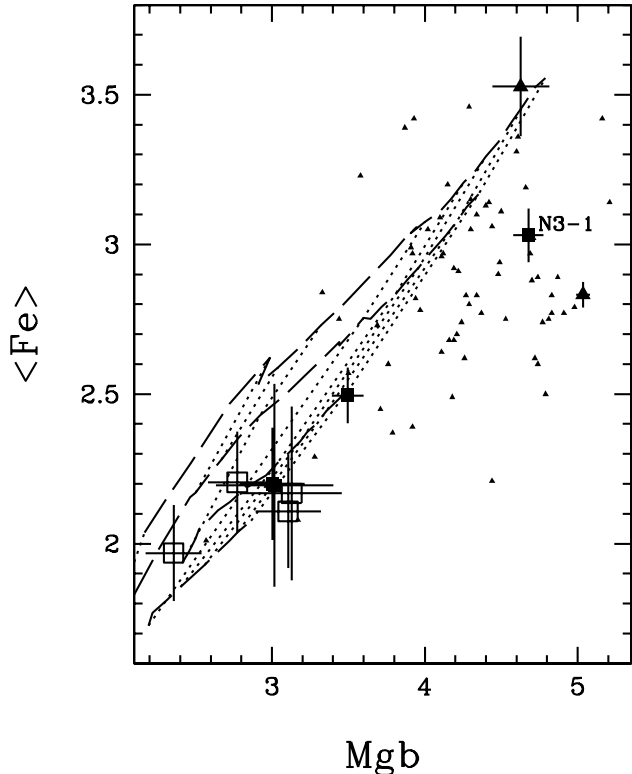


FIG. 8.— The $\langle \text{Fe} \rangle$ index vs. the Mgb index. Filled boxes: LSB galaxies with no $\text{H}\beta$ emission; Open boxes: LSB galaxies with measured $\text{H}\beta$ emission; Large triangles: our data of HSB ellipticals; small triangles: Coma cluster elliptical and S0 galaxies from Jørgensen (1999). The same models used for the grid in Figure 7 are used here. The Mgb and $\langle \text{Fe} \rangle$ indices have similar sensitivity to age and metallicity, so the model grid is very narrow. N3-1, like many of elliptical galaxies, lies off the model grid, suggesting super-solar $[\text{Mg}/\text{Fe}]$ abundance. See the text for details.

McGaugh (1994), in his study of LSB galaxy H II regions, found evidence for dust in some galaxies, with internal extinctions as high as $E(B-V) \sim 0.5$ (corresponding to $E(B-I_c) \sim 1.3$). The galaxies in that study were similar to the lower metallicity galaxies ($[\text{N II}]/\text{H}\alpha < 0.2$) in Figure 11a for which we find a similar range of reddenings. His study did not include any of the red or giant LSB galaxies for which we find generally larger reddening values.

The dust distribution in galaxies tends to be clumped, and these reddening values apply only to the regions where the emission lines are produced. The emission line regions and light from the stellar disk are not spatially resolved in our observations and both contribute to the extracted spectra. Consequently, we cannot constrain the reddening affecting the general stellar disk, which dominates the continuum luminosity of the galaxy, and thus we do not make a correction to the global photometry for internal extinction.

Figure 11a shows a trend for the Balmer ratio (and presumed reddening) to increase with increasing gas-phase metallicity. In Figure 11(b-d) we plot the Balmer ratio versus photometric parameters dominated by the stellar disk. There is no correlation at all between $\text{H}\alpha/\text{H}\beta$ and central surface brightness over the range $22 \leq \mu_B(0)_{\text{cor}} \leq 25$, nor is there a correlation between $\text{H}\alpha/\text{H}\beta$ and galaxy incli-

nation. The correlation between $(B-I_c)_{\text{tot}}$ color and the Balmer ratio is shown for the NFGS galaxies in Figure 11d. The LSB galaxies fall onto the same locus of points, especially after applying a correction for underlying $\text{H}\alpha$ absorption of 1.5 Å. The LSB galaxies appear to lie along the reddening vector in Figure 11d. This might imply that the dust is not local to the emission region, but is instead mixed throughout the galaxy. Alternatively, it is possible that the colors are not caused by dust reddening of the stellar light, and the relation between $\text{H}\alpha/\text{H}\beta$ and $(B-I_c)_{\text{tot}}$ is not the fundamental one. Rather, the amount of dust increases with increasing metallicity (Fig. 11a), and the stellar populations also become redder with increasing metallicity (cf. the tight correlation between $[\text{N II}]/\text{H}\alpha$ and $(B-I_c)_{\text{tot}}$ shown on Fig. 12c, and the corresponding discussion in Section 8), which in turn results in the correlation seen here between $\text{H}\alpha/\text{H}\beta$ and $(B-I_c)_{\text{tot}}$. If the colors are driven by dust reddening over the whole galaxy, then we would expect to also see a correlation between galaxy inclination and reddening, with higher reddening measurements for galaxies closer to edge-on. We do not detect any such correlation, and thus conclude that the correlation between $\text{H}\alpha/\text{H}\beta$ and $(B-I_c)_{\text{tot}}$ is secondary, and both parameters are driven primarily by the metallicity.

Regardless of the interpretation of the galaxy colors, it is clear that dust is present in abundance in some LSB galaxies, particularly the red and high metallicity ones, but the absence of a correlation between dust and $\mu_B(0)_{\text{cor}}$ suggests that dust is not the cause of the low surface brightness for LSB galaxies of any color.

The relative emission line strengths presented in Table 7 have not been corrected for internal extinction within these galaxies. The line ratios we use in our analysis (e.g. $[\text{N II}]/\text{H}\alpha$) all have narrow wavelength spreads, and are not significantly affected by dust in the amount we detect. The uncertainty of a correction for intrinsic reddening, however, would be significantly larger than the correction itself (which is negligible), and so we do not apply any correction.

8. EMISSION LINE PROPERTIES VERSUS GLOBAL PHOTOMETRIC PROPERTIES

In Figure 12, we show $[\text{N II}]/\text{H}\alpha$ and $\text{EW}(\text{H}\alpha)$ versus central surface brightness, absolute magnitude, and $(B-I_c)_{\text{tot}}$. We plot the absorption line galaxies in this figure as well, using the $[\text{N II}]/\text{H}\alpha$ values derived and discussed in Section 6. However, these four galaxies are never included when we measure correlations between the parameters plotted in Figure 12.

In Figures 12c and 12f, the outlier P9-4 at $(B-I_c)=2.33$ (OBSCI97) is purportedly the reddest object in the sample, despite its high $\text{EW}(\text{H}\alpha)$ and metal poor nature. The continuum slope in our HET spectrum of this object is very flat. In comparison, the galaxies at $(B-I_c)=1.3$ have bluer continua, but those at $(B-I_c)=1.8$ have redder continua. The continuum slope of N10-2 ($B-I_c=1.48$) is also very flat. We suggest that there are errors in the published photometry for P9-4. We label P9-4 in all panels of Figure 12 and we do not include the data for P9-4 in the determination of any of the correlations discussed below.

Figures 12a and 12d show that there is a broad range of both $[\text{N II}]/\text{H}\alpha$ and $\text{EW}(\text{H}\alpha)$ values for the whole range

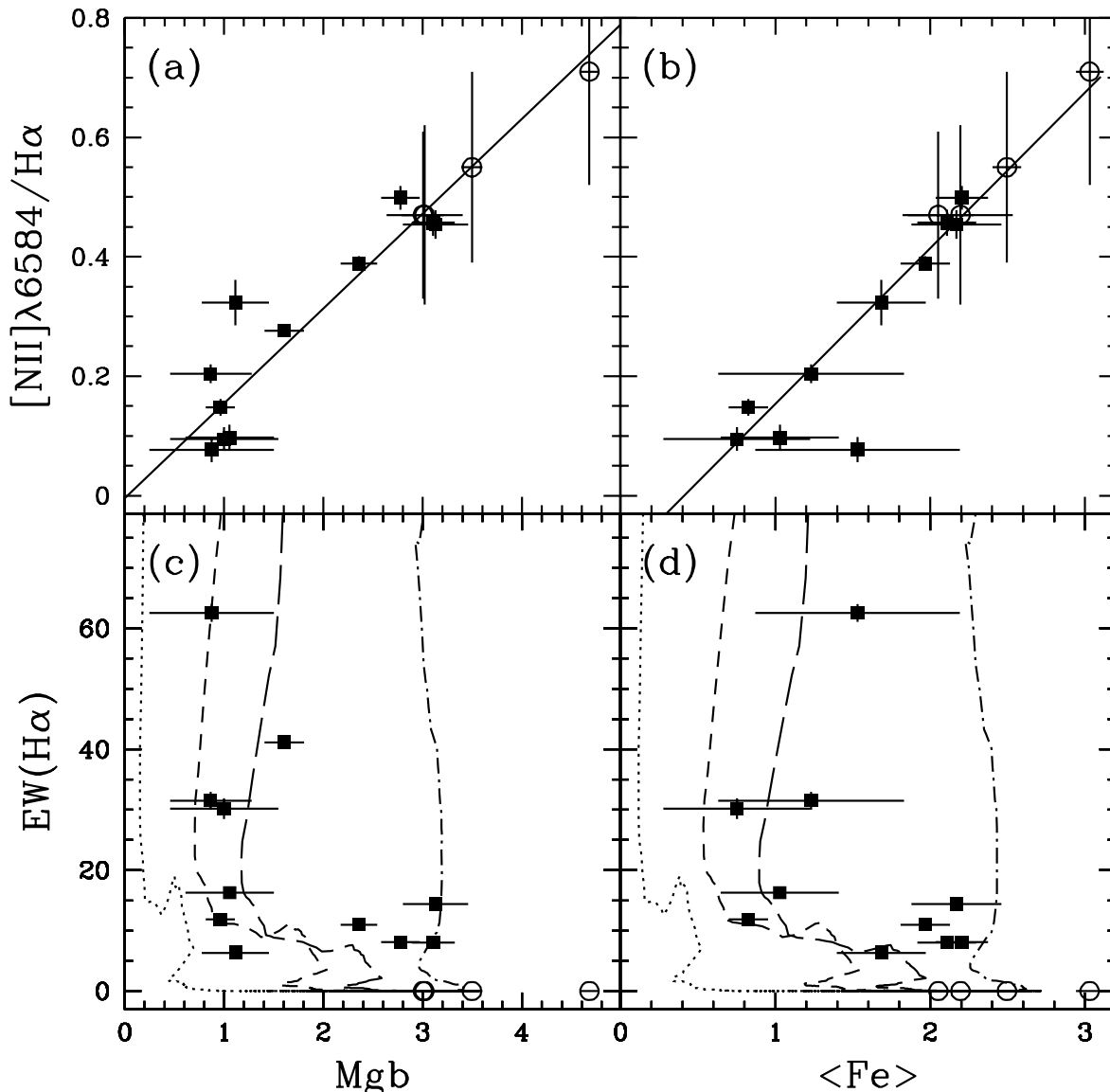


FIG. 9.— Comparison of gas phase indicators and stellar absorption line indices. The gas phase $[\text{N II}]/\text{H}\alpha$ ratio plotted against (a) the stellar Mgb line index and (b) the $\langle \text{Fe} \rangle$ line index. The best fitting relations are shown as solid lines. (c) The $\text{EW}(\text{H}\alpha)$ vs. the Mgb index. (d) $\text{EW}(\text{H}\alpha)$ vs. the $\langle \text{Fe} \rangle$ index. Boxes: LSB galaxies with measured emission lines; circles: LSB galaxies with no measured emission, see Section 6 for details. The lines in panels (c) and (d) are evolutionary tracks for an old-plus-burst stellar population, with a 5 Gyr old population, and bursts which comprise (from left to right) of 10% (dotted), 2% (short-dash), 1% (long-dash) and 0.1% (dot-dash) of the total stellar mass. The kink in these evolutionary tracks occurs at ~ 7.5 Myr after the burst, and the $\text{EW}(\text{H}\alpha)$ drops below 1 \AA within 20 Myr of the burst for all the tracks. The tracks all end at $\text{Mgb} = 3.6$ and $\langle \text{Fe} \rangle = 2.7$, $\text{EW}(\text{H}\alpha) \simeq 0$, which are the values of the underlying population.

of surface brightnesses studied. A Kendall's τ test gives a probability of 54% that there is no correlation between $\text{EW}(\text{H}\alpha)$ and $\mu_{\text{B}}(0)_{\text{cor}}$. There is a probability of 31% that there is no correlation between $[\text{N II}]/\text{H}\alpha$ and $\mu_{\text{B}}(0)_{\text{cor}}$. In contrast, Bell & de Jong (2000) found correlations both between mean age and K-band central surface brightness, and between mean metallicity and K-band central surface brightness. Their modelling involved an assumption of exponentially decreasing star formation rates all beginning at the same time in the past (12 Gyr), with different exponential timescales, τ , which thus produced stel-

lar populations with different luminosity-weighted mean ages at the current epoch. They varied τ and metallicity in their models to produce a grid in the $(R_c - K)$ vs. $(B - I_c)$ plane, which was then used to interpret their data. These models have a very similar SFH to the models of Kennicutt et al. (1994), which we use for the right side scale on Figure 12(d-f) and which predict a monotonic relationship between $\text{EW}(\text{H}\alpha)$ and τ , and consequently mean age. However, as mentioned above, we do not see a correlation between $\text{EW}(\text{H}\alpha)$ and B-band central surface brightness. Bell & de Jong make an unweighted least-

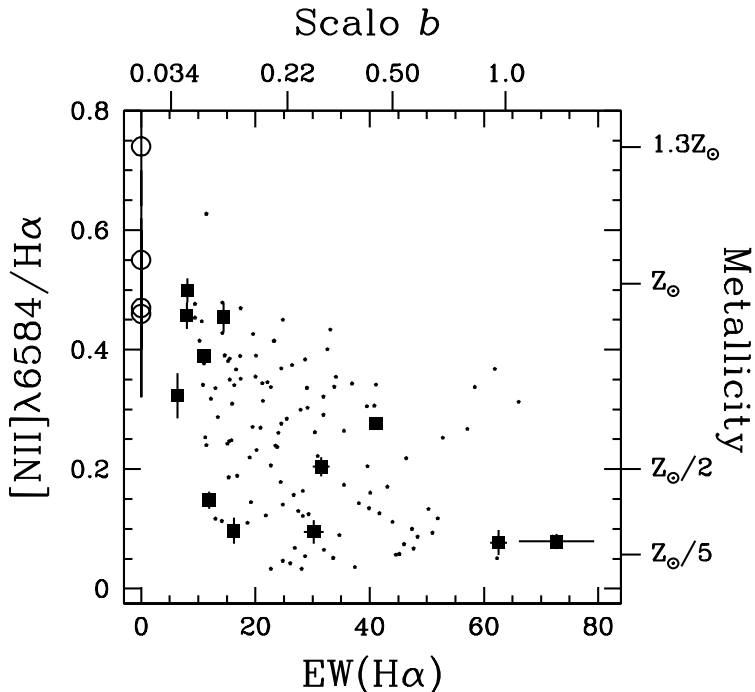


FIG. 10.— The metallicity indicator $[\text{N II}]/\text{H}\alpha$ plotted against $\text{EW}(\text{H}\alpha)$, a measure of the birthrate parameter. Large boxes: LSB galaxies with measured emission lines; circles: LSB galaxies with no measurable emission lines whose positions are based on the extrapolation described in Section 6; small boxes: HSB galaxies from the NFGS (Jansen et al. 2000). The right axis shows the $[\text{N II}]/\text{H}\alpha$ metallicity calibration of Denicoló et al. (2002), appropriate for H II regions. The top axis shows the $\text{EW}(\text{H}\alpha)$ calibration of the Scalo birthrate parameter for one star formation model detailed in Kennicutt et al. (1994). See text for details.

squares fit to their data which produces a change in mean age of 0.84 ± 0.08 Gyr for a change of two magnitudes in central surface brightness, equivalent to the range covered by our sample, with lower luminosity-weighted mean ages occurring at lower central surface brightness. Their fit to the metallicity-surface brightness relation produced a change in the mean metallicity of 0.26 dex for the same two magnitude change in central surface brightness, with higher metallicity at higher surface brightness. Our sample size, though similar to the LSB galaxy study of Bell et al. (2000), is a small fraction of the combined HSB-plus-LSB galaxy sample of Bell & de Jong. It is quite possible that our sample selection, which deliberately covers a wide range of galaxy colors and surface brightnesses, has led to more scatter than would be present in a volume-limited sample of galaxies, and that therefore we might not be sensitive to these predicted modest changes in mean age and metallicity.

The line ratio $[\text{N II}]/\text{H}\alpha$ versus the absolute magnitude is shown in Figure 12b. This plot makes clear the point that LSB galaxies are not synonymous with dwarf galaxies, but cover a range of absolute magnitudes comparable to that of HSB galaxies. The emission line LSB galaxies show a correlation between $[\text{N II}]/\text{H}\alpha$ and absolute magnitude. A Kendall’s τ test gives a probability of 5% that no correlation is present. The relation for LSB galaxies matches that of the NFGS galaxies. The LSB galaxies without

emission also follow the correlation, but form a ridge on the faint, high metallicity edge of the galaxy distribution. This may be reflecting a higher B-band mass-to-light ratio in these older objects, if the $[\text{N II}]/\text{H}\alpha$ - M_{Btot} relation is a result of a more fundamental metallicity-mass relation. Alternatively, it could reflect a systematic error in the interpolation/extrapolation of the $[\text{N II}]/\text{H}\alpha$ -Mgb and $[\text{N II}]/\text{H}\alpha$ - $\langle \text{Fe} \rangle$ relations used for the non-star-forming galaxies.

The distribution of the LSB galaxies is a good match to that of the NFGS galaxies in Figure 12e. We do not detect any correlation between $\text{EW}(\text{H}\alpha)$ and M_{Btot} . A Kendall’s τ test gives a probability of 63% that there is no correlation for the emission line LSB galaxies. A rough scaling of the absolute SFR can be determined by multiplying the $\text{EW}(\text{H}\alpha)$ by the total R-band luminosity, which includes the continuum near $\text{H}\alpha$. Within our sample, the galaxies with the largest $(\text{EW}(\text{H}\alpha) \cdot L_{\text{B}})$ are the ones at the higher surface brightness end of our range, with $\mu_{\text{B}}(0)_{\text{cor}} \lesssim 23.0$ mag/arcsec². Galaxies with lower total SFR will be found in the lower right of the $\text{EW}(\text{H}\alpha)$ vs. M_{Btot} diagram. Our sample selection is neither complete nor representative, so we cannot comment on how the absolute star-formation rates of LSB and HSB galaxies compare. van den Hoek et al. (2000) found that the mean present-day SFR for a sample of late-type LSB galaxies was about one-tenth the SFR of similar HSB galaxies.

The relations between $[\text{N II}]/\text{H}\alpha$ and $\text{EW}(\text{H}\alpha)$ with $(\text{B}-\text{I}_{\text{c}})$ color, shown in Figs. 12c and 12f, are comparable in strength to those between $[\text{N II}]/\text{H}\alpha$ and the stellar absorption indices Mgb and $\langle \text{Fe} \rangle$. A Kendall’s τ test applied to the emission line LSB galaxies gives a probability of 2% that there is no correlation between $[\text{N II}]/\text{H}\alpha$ and $(\text{B}-\text{I}_{\text{c}})_{\text{tot}}$. Similarly, there is a probability of only 0.7% that $\text{EW}(\text{H}\alpha)$ and $(\text{B}-\text{I}_{\text{c}})_{\text{tot}}$ are not correlated for the emission line LSB galaxies. $(\text{B}-\text{I}_{\text{c}})$ color is sensitive to changes in age, metallicity, and dust reddening, and all three may play some role in explaining the correlations. If we use the Denicoló et al. (2002) calibration for $[\text{N II}]/\text{H}\alpha$, the resulting metallicity range spanned by the data is less than one dex. At any constant age less than 5 Gyr, the V2000 stellar population models predict a maximum $(\text{B}-\text{I}_{\text{c}})$ color range of only 0.6 mag for a range in $[\text{Fe}/\text{H}]$ from -1.0 dex to +0.2 dex. The $(\text{B}-\text{I}_{\text{c}})_{\text{tot}}$ range spanned by our data is more than one magnitude, so varying only the metallicity of the stellar population is not a sufficient explanation for the colors. Stellar populations with mean ages older than 5 Gyr will show a wider color range over that range of metallicity, but are not supported by the ages determined in Section 5 for the four absorption line dominated LSB galaxies.

Including age in the interpretation of the colors requires us to make assumptions about the SFH in these galaxies. In Section 6, we discussed three plausible star formation scenarios: (1) continuous, but decreasing star formation rate with a build-up of metallicity, (2) old-plus-burst models with an old stellar population underlying a significant ($> 1\%$ by mass) burst of star formation, and (3) old-plus-burst SFH models where the burst was small ($< 0.3\%$ by mass) and produced $\text{H}\alpha$ emission, but had little effect on the global photometric properties. Scenario (2) was rejected because it would not maintain the strong correlation

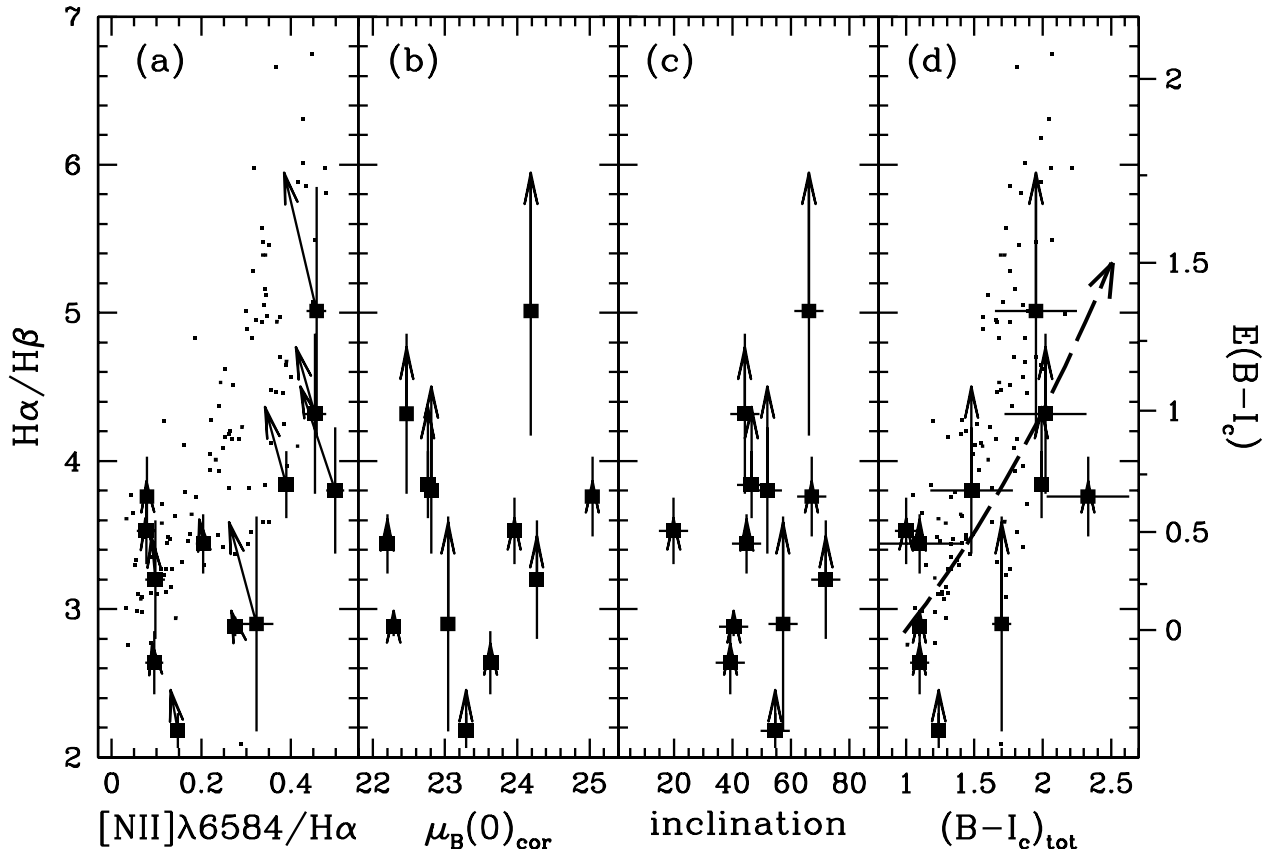


FIG. 11.— The Balmer ratio, $H\alpha/H\beta$, plotted against (a) the metallicity indicator $[N II]\lambda 6584/H\alpha$, (b) the central surface brightness $\mu_B(0)_{\text{cor}}$, (c) galaxy inclination (edge-on = 90°), and (d) The total $(B-I_c)$ color. Large boxes – LSB galaxies; small points – galaxies from the NFGS (Jansen et al. 2000). The right side y-axis lists the $E(B-I_c)$ values derived from equation 3. The vertical arrows show where the LSB galaxies would move if we made a correction of 1.5 \AA to the $H\alpha$ equivalent width to account for underlying stellar absorption. The dashed arrow in panel (d) shows the locus of reddening vectors for the LSB galaxies. The reddening vector for the NFGS galaxies (whose colors have been transformed from observed $(B-R_c)$ colors) would be $\approx 10\%$ steeper. The uncertainties shown for the Balmer ratios do not include those caused by uncertainties in the absorption correction to $H\beta$. The NFGS data has not been corrected for underlying stellar absorption at $H\alpha$ or $H\beta$. Applying an arbitrary correction of 1.5 \AA to the equivalent width of both $H\alpha$ and $H\beta$ does not significantly shift the location of the locus of HSB galaxy points.

between $[N II]/H\alpha$ and M_{gb} or $\langle Fe \rangle$. Scenario (3) was acceptable simply because the blue flux from the young population did not significantly veil the strength of the underlying metal absorption strength, and the $[N II]/H\alpha$ - metal index correlations were unperturbed. However, this assumption also means that the global colors will not be significantly changed by the young burst. Consequently, for this SFH we must invoke a screen of dust as the explanation for the large range of $(B-I_c)$ colors. Scenario (1) predicts a correlation between age and metallicity, which then produces a tight correlation between metallicity and the M_{gb} , $\langle Fe \rangle$ strengths for the stellar population. By invoking a correlated evolution of age and metallicity, we avoid adding scatter to parameters affected by both, including color. Furthermore, the range of $(B-I_c)$ colors in this picture is at least as great as the range seen in our data. The V2000 models for a 1 Gyr population with one-fifth solar metallicity predict $(B-I_c)=1.57$, while a 4 Gyr solar metallicity stellar population would have $(B-I_c)=2.55$. Mean ages less than 1 Gyr yield colors bluer than $(B-I_c)=1.5$, and while the zeropoint of the model colors is poorly calibrated, the range is more accurate. Dust,

while certainly present in the emission line regions, is not necessary to explain the global colors in this scenario.

9. DISCUSSION

The previous sections show that LSB galaxies cover a wide range of metallicities, and as a class they may contain both old and young stellar populations. Dust is present in some LSB galaxies, and may affect their global colors. Star formation occurs continuously in these galaxies, but with global rates which have varied exponential decay timescales. The metallicities of the galaxies are coupled to their ages, such that galaxies with older mean ages have reached a higher metallicity. Bursts that occur after long periods without star formation must make up a very small fraction of the total galaxy mass.

The detailed study of LSB galaxies is still a young field, partly because the observations are very difficult to make. The study of LSB galaxies originated with the realization that selection effects in imaging surveys had an impact on our understanding of the galaxy population, and galaxy formation and evolution in general. While we are now more conscious of some of the biases, samples chosen for

follow-up study are still subject to selection effects. It is interesting to look at the studies in the literature in the context of our results, and determine what effects selection or observational biases have had on both our and the published conclusions.

Previous spectroscopic studies of LSB galaxy chemical abundances (McGaugh 1994; Rönback & Bergvall 1995; de Blok & van der Hulst 1998) were done on galaxies selected to have at least one bright H II region. These studies concluded that LSB galaxies were all metal-poor, with gas phase metal abundance less than one-tenth to one-fifth solar. These galaxies were selected from photographic surveys which were much more sensitive to blue galaxies than red galaxies at the surface brightness limit. Furthermore, the H II regions selected were the brightest H II regions in the galaxy, and lower metallicity H II regions will have higher ionization parameters and be brighter than high metallicity H II regions with similar numbers and ages of stars. Compared to our sample, and based on the implicit color criterion imposed by the photographic surveys, these studies were limited to having galaxies as blue or bluer than the five bluest galaxies in our survey. The five bluest galaxies in our study (C5-3, N9-1, U1-4, C4-1, and P1-3) all have active star formation, and define the low metallicity end of the sample. Though they do overlap the range of surface brightnesses and total absolute magnitudes covered by the rest of our sample, they are certainly not representative of the full continuum of LSB galaxy properties found for the sample.

Gerritsen & de Blok (1999) made an N-body simulation of the SFH for one of the blue late-type LSB galaxies from de Blok & van der Hulst (1998), and found that they required both low mass surface density and low metallicity to explain the properties of the galaxy. The SFH they derived has a slowly decreasing SFR when averaged over timescales of order 100 Myr, but has significant (factors of 2) deviations from the mean SFR on timescales of order 20 Myr. It is these deviations from the mean, they say, which explains the color range seen for LSB galaxies in general. Their models do not predict absorption line strengths, but if the colors are significantly affected by the SFR deviations, then the Mgb and $\langle \text{Fe} \rangle$ absorption line indices must also be affected. Their simulation cannot be used to explain the full range of LSB galaxy parameters that we see. First of all, despite some uncertainty in the metallicity zeropoints of the $[\text{N II}]/\text{H}\alpha$, Mgb and $\langle \text{Fe} \rangle$ indicators, we find LSB galaxies with metallicities near solar, and certainly at least half-solar. Their models require metallicities less than about one-fifth solar to maintain a low SFR. Furthermore, the range of color (and we infer also Mgb, $\langle \text{Fe} \rangle$) is decoupled from increases in metallicity, in conflict with the $[\text{N II}]/\text{H}\alpha$ -Mgb, $[\text{N II}]/\text{H}\alpha$ - $\langle \text{Fe} \rangle$, and $[\text{N II}]/\text{H}\alpha$ -(B-I_c) correlations. Determining whether the range of colors (and thus Mgb and $\langle \text{Fe} \rangle$) they predict at any given metallicity could be hidden within the scatter of these correlations requires more quantitative modelling than we have done. The Gerritsen & de Blok models predict that $\sim 20\%$ of the late-type LSB galaxy population will have red colors, (B-V) ~ 1 . However, those galaxies should be gas rich and metal-poor, and while the gas fractions of the red LSB galaxies in our sample remain unconstrained, their metallicities are higher than predicted

by Gerritsen & de Blok. In addition, they predict that these red galaxies will have $\mu_{\text{B}}(0) \simeq 24.5 \text{ mag}/\square''$, which is fainter than the galaxies selected for our sample. This surface brightness is well below the completeness limit of the OBC97 survey, and no other large surveys for red LSB galaxies have yet been published.

van den Hoek et al. (2000) modeled the SFH of the galaxies studied by de Blok & van der Hulst (1998) using a galactic chemical and photometric evolution model. They were able to explain the colors, magnitudes, and gas phase metallicities of most of the blue LSB galaxies with a SFH that had a continuous, exponentially decreasing SFR over a period of 14 Gyr. For the bluest galaxies in the sample (with (B-V) < 0.45) an additional burst of star formation was needed. While our analysis rejects the possibility for significant late-time, i.e. high metallicity, bursts, none of the galaxies in our sample are that blue.

Bell et al. (2000) used near-infrared and optical colors to study the stellar populations of blue, red, and giant LSB galaxies. They did not require that the galaxies have H II regions, nor that they had previous detections in H I. However, their sample did have a higher average surface brightness than the spectroscopic studies, so that they could get sufficient S/N in the K-band imaging. Their sample has a similar central surface brightness distribution to ours. Like us, they found that LSB galaxies cover a range of metallicities, with some having metallicities near solar. They also found that some red LSB galaxies had rather old luminosity-weighted mean ages. They only had five red LSB galaxies in their survey and they determined that those with old ages and solar metallicities were all at the bright end of the LSB surface brightness range, $\mu_{\text{B}}(0) \sim 22.5 \text{ mag}/\square''$. We find old, metal rich stellar populations in some red galaxies with $\mu_{\text{B}}(0) \simeq 24.0 \text{ mag}/\square''$. By combining the Bell et al. LSB sample with a sample of HSB disk galaxies, Bell & de Jong (2000) found a clear correlation between mean age and surface brightness, which we do not detect. The discrepancies in both cases can be explained by small sample sizes, especially of the reddest LSB galaxies in the sample.

Impey et al. (2001) obtained low resolution ($\cong 20\text{\AA}$), low S/N optical spectra for 250 galaxies selected from the APM survey of Impey et al. (1996), 93 of which have central surface brightnesses fainter than $\mu_{\text{B}} = 22 \text{ mag}/\square''$ (their LSB cutoff). They also obtained HI spectra for 145 LSB galaxies. Burkholder et al. (2001) analyze these data, and measure Balmer decrements ($\text{H}\alpha/\text{H}\beta$) and $[\text{O}/\text{H}]$ (using the R₂₃ method) when the optical spectra are of sufficient quality (43 HSB and 17 LSB galaxies have measured $[\text{O}/\text{H}]$). They also measure the best-fit Tully-Fisher relation for the HI sample. Their sample selection criteria were similar to those of Bell et al. (2000) and ourselves: no requirements for prior HI detections, or the presence of HII regions. Though the quality of their data for individual galaxies may not be as good, they have a larger dataset to draw conclusions from, and their conclusions match ours: there is evidence for old stellar populations in some LSB galaxies, and the range of metallicities for LSB galaxies shows a large overlap with the range of metallicities seen in HSB galaxies.

A complete picture of the formation and evolution of LSB galaxies is still not in hand, as many of the conclu-

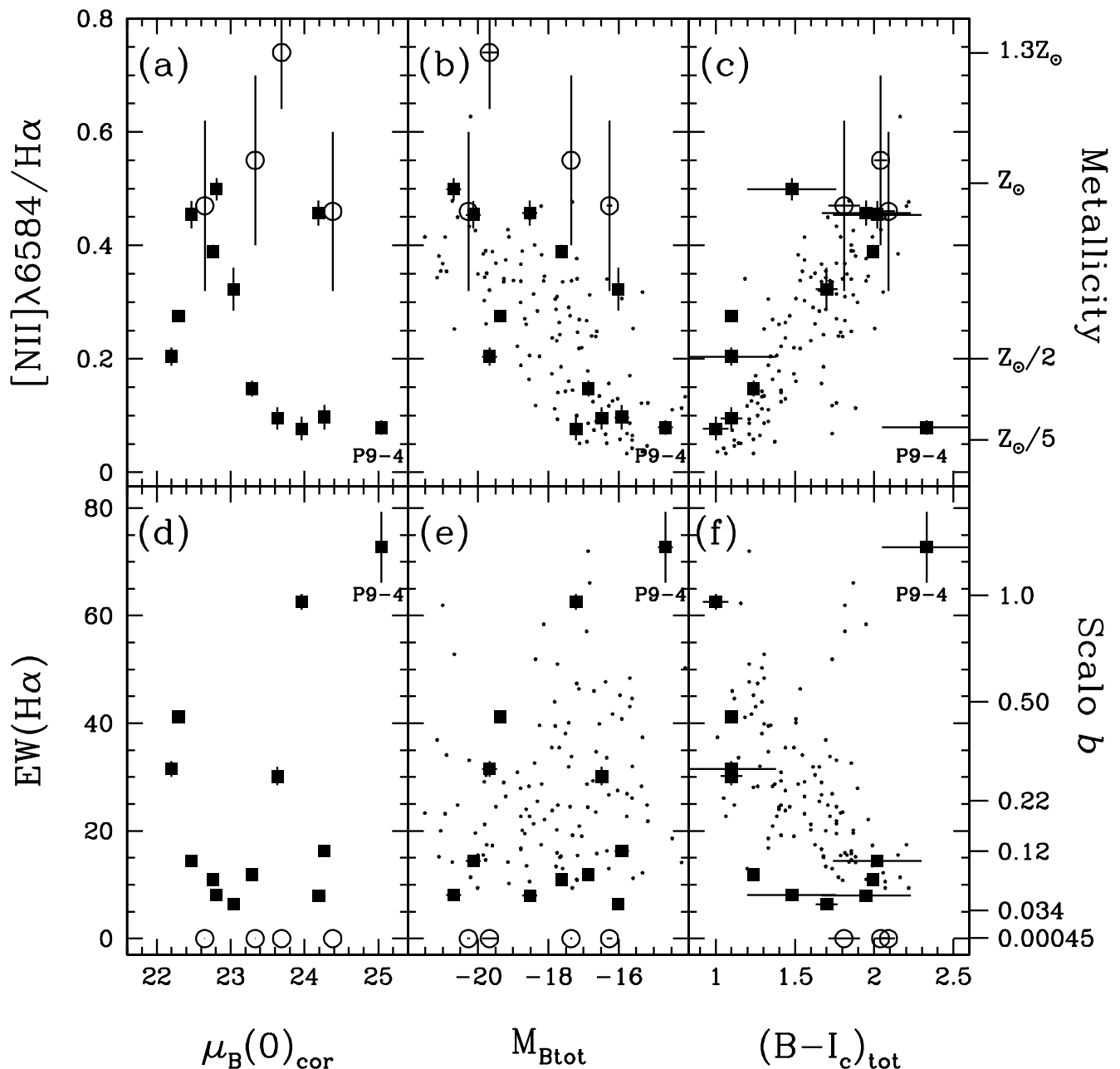


FIG. 12.— The metallicity indicator $[\text{N II}]/\text{H}\alpha$ and the age indicator $\text{EW}(\text{H}\alpha)$ plotted against central surface brightness, $\mu_{\text{B}}(0)_{\text{cor}}$, absolute magnitude, M_{Btot} , and $(\text{B}-\text{I}_c)$ color. Large boxes: LSB galaxies with measured emission lines; circles: LSB galaxies with no measured emission lines; small pentagons: emission line galaxies in the NFGS (Jansen et al. 2000). On the right side axes are the metallicity and birthrate parameter calibrations described in Section 6. The correlation between metallicity and absolute magnitude found for HSB emission-line galaxies is also seen in LSB galaxies. We do not detect a significant correlation between metallicity and surface brightness in this sample. The strongest correlation is between color and $[\text{N II}]/\text{H}\alpha$. See text for comments on the published photometry for P9-4.

sions of these authors and ourselves are clearly still subject to variance due to small and incomplete samples. Future detailed studies should rely on deep, complete, multi-color surveys with well determined detection criteria to gain a better overall picture of LSB galaxy formation and evolution. The constraints on LSB SFH implied by the many correlations we detect are only applicable to LSB galaxies with $1.0 < (\text{B} - \text{I}_c) < 2.1$ and $\mu_{\text{B}}(0) < 24.3 \text{ mag}/\square''$.

10. SUMMARY & CONCLUSIONS

We have used the Marcario Low Resolution Spectrograph on the 9.2m Hobby-Eberly Telescope to obtain deep integrated spectra of the gaseous and stellar components of 19 LSB galaxies, covering a range of colors and surface brightnesses. These spectra have sufficient spectral resolution and S/N in the continuum to measure both emission line ratios and stellar absorption line strengths.

The spectra of these galaxies qualitatively resemble the spectra of HSB galaxies covering the full range of spectra seen in galaxies of Hubble types from E to Irr. In most of

the parameters we measure, LSB galaxy properties cover the same broad range as HSB galaxies. Four galaxies have spectra whose features are dominated by old stellar populations, covering a range of abundances from less than half solar to twice solar metallicity. None of these four have been detected in H I. The remainder of the galaxies show evidence for ongoing star formation, in some cases at a significant rate compared to their average past SFR. At least one massive red LSB galaxy shows evidence for super-solar [Mg/Fe] abundance. This is in accord with similar findings for HSB galaxies, and suggests that the mechanism responsible for the super-solar abundance ratios is effective in LSB galaxies as well. All of the emission line galaxies are consistent with star formation, rather than AGN, being the ionizing source.

There are tight correlations between the stellar absorption line indices and the gas phase indicators $[N II]/H\alpha$ and $EW(H\alpha)$. These have not been studied before, in LSB or HSB galaxies. We use these correlations to argue that the SFH for these galaxies must be fairly smooth. Large bursts of star formation, or multiple small bursts separated by long quiescent periods, do not fit these relations.

Dust is present in some of these galaxies, with A_V as large as 1.8 mags. We are unable to determine, though, whether the dust is isolated to the emission line regions, or if it is mixed in with the stellar population.

The redshift distribution for this galaxy sample is very broad, ranging from 3000 to 70000 km/s. Additionally, we find several discrepancies between the published redshifts based on Arecibo 305m telescope H I observations and our new optical observations. In most cases, the discrepancy can be explained by beam confusion affecting the Arecibo detection. All of the galaxies found by O'Neil et al. (2000a) to deviate significantly from the Tully-Fisher relation, we show to suffer from significant redshift errors.

ACKNOWLEDGEMENTS

We would like to thank the staff of the Hobby-Eberly telescope for obtaining the data, and we heartily thank the many astronomers and engineers involved in building the telescope and its instruments. We thank Greg Shields for useful discussions on nebular chemical abundances, and Karl Gebhardt for comments on an early draft of this paper. We also thank the anonymous referee for comments which helped to improve this paper. The Hobby-Eberly Telescope is operated by McDonald Observatory on behalf of The University of Texas at Austin, the Pennsylvania State University, Stanford University, Ludwig-Maximilians-Universität München, and Georg-August-Universität Göttingen. The Marcario Low Resolution Spectrograph is a joint project of the Hobby-Eberly Telescope partnership and the Instituto de Astronomia de la Universidad Nacional Autonoma de México. This material is based in part upon work supported by the Texas Advanced Research Program under Grant No. 009658-0060-1977. This research was supported in part by the Gemini Observatory, which is operated by the Association of Universities for Research in Astronomy, Inc., on behalf of the international Gemini partnership of Argentina, Australia, Brazil, Canada, Chile, the United Kingdom, and the United States of America. This research has made use of the NASA/IPAC Extragalactic Database (NED) which

is operated by the Jet Propulsion Laboratory, California Institute of Technology, under contract with the National Aeronautics and Space Administration. This research has made use of NASA's Astrophysics Data System Service.

REFERENCES

- Bell, E. F., Barnaby, D., Bower, R. G., de Jong, R. S., Harper, D. A., Hereld, M., Loewenstein, R. F., & Rauscher, B. J. 2000, *MNRAS*, 312, 470
- Bell, E. F. & de Jong, R. S. 2000, *MNRAS*, 312, 497
- Bertin, E. & Arnouts, S. 1996, *A&AS*, 117, 393
- Burkholder, V., Impey, C., & Sprayberry, D. 2001, *AJ*, 122, 2318
- Burstein, D. & Heiles, C. 1982, *AJ*, 87, 1165
- Cardelli, J. A., Clayton, G. C., & Mathis, J. S. 1989, *ApJ*, 345, 245
- Chromey, F. R. & Hasselbacher, D. A. 1996, *PASP*, 108, 944
- Chung, A., van Gorkom, J. H., O'Neil, K., & Bothun, G. 2002, *AJ*, 123, 2387
- Claver, C. F. 1995, Ph.D. Thesis, University of Texas, Austin
- Cross, N. & Driver, S. P. 2002, *MNRAS*, 329, 579
- Dalcanton, J. J., Spergel, D. N., Gunn, J. E., Schmidt, M., & Schneider, D. P. 1997, *AJ*, 114, 635
- Davies, R. L., Burstein, D., Dressler, A., Faber, S. M., Lynden-Bell, D., Terlevich, R. J., & Wegner, G. 1987, *ApJS*, 64, 581.
- Davies, R. L., Sadler, E. M., & Peletier, R. F. 1993, *MNRAS*, 262, 650.
- de Blok, W. J. G. 1997, Ph.D. Thesis, Rijksuniversiteit Groningen
- de Blok, W. J. G. & McGaugh, S. S. 1997, *MNRAS*, 290, 533
- de Blok, W. J. G., McGaugh, S. S., & van der Hulst, J. M. 1996, *MNRAS*, 283, 18
- de Blok, W. J. G. & van der Hulst, J. M. 1998, *A&A*, 335, 421
- de Blok, W. J. G., van der Hulst, J. M., & Bothun, G. D. 1995, *MNRAS*, 274, 235
- de Jong, R. S. & Lacey, C. 2000, *ApJ*, 545, 781
- Denicoló, G., Terlevich, R., & Terlevich, E. 2002, *MNRAS*, 330, 69.
- Falco, E. E. et al. 1999, *PASP*, 111, 438 (UZC)
- Freeman, K. C. 1970, *ApJ*, 160, 811
- Frei, Z. & Gunn, J. E. 1994, *AJ*, 108, 1476
- Fukugita, M., Shimasaku, K., & Ichikawa, T. 1995, *PASP*, 107, 945.
- Gerritsen, J. P. E. & de Blok, W. J. G. 1999, *A&A*, 342, 655
- Goudfrooij, P. & Emsellem, E. 1996, *A&A*, 306, L45
- Hill, G. J., Nicklas, H. E., MacQueen, P. J., Tejada, C., Cobos Duenas, F. J., & Mitsch, W. 1998, *Proc. SPIE*, 3355, 375.
- Impey, C., Burkholder, V., & Sprayberry, D. 2001, *AJ*, 122, 2341
- Impey, C. D., Sprayberry, D., Irwin, M. J., & Bothun, G. D. 1996, *ApJS*, 105, 209
- Jansen, R. A., Fabricant, D., Franx, M., & Caldwell, N. 2000, *ApJS*, 126, 331
- Jørgensen, I. 1997, *MNRAS*, 288, 161.
- Jørgensen, I. 1999, *MNRAS*, 306, 607
- Kennicutt, R. C. 1992, *ApJ*, 388, 310.
- Kennicutt, R. C. 1998, *ARA&A*, 36, 189
- Kennicutt, R. C., Tamblyn, P., & Congdon, C. E. 1994, *ApJ*, 435, 22
- Kewley, L. J. & Dopita, M. A. 2002, *ApJsubmitted*
- Kewley, L. J., Dopita, M. A., Sutherland, R. S., Heisler, C. A., & Trevena, J. 2001a, *ApJ*, 556, 121
- Kewley, L. J., Heisler, C. A., Dopita, M. A., & Lumsden, S. 2001b, *ApJS*, 132, 37
- Kilborn, V. A. et al. 2000, *AJ*, 120, 1342
- Kobulnicky, H. A., Kennicutt, R. C., & Pizagno, J. L. 1999, *ApJ*, 514, 544
- Kobulnicky, H. A. & Skillman, E. D. 1997, *ApJ*, 489, 636
- Kuntschner, H., Lucey, J. R., Smith, R. J., Hudson, M. J., & Davies, R. L. 2001, *MNRAS*, 323, 615.
- Landolt, A. U. 1992, *AJ*, 104, 340
- Leitherer, C. et al. 1999, *ApJS*, 123, 3
- Maraston, C. & Thomas, D. 2000, *ApJ*, 541, 126
- Matthews, L. D. & Gao, Y. 2001, *ApJ*, 549, L191
- McGaugh, S. S. 1991, *ApJ*, 380, 140
- McGaugh, S. S. 1994, *ApJ*, 426, 135
- McGaugh, S. S., Bothun, G. D., & Schombert, J. M. 1995, *AJ*, 110, 573
- McGaugh, S. S., Rubin, V. C., & de Blok, W. J. G. 2001, *AJ*, 122, 2381
- Monet, D., et al. 1998, *The USNO-SA2.0 Catalog* (Washington: US Naval Obs.)
- Nilson, P. 1973, *Acta Universitatis Upsaliensis. Nova Acta Regiae Societatis Scientiarum Upsaliensis - Uppsala Astronomiska Observatoriums Annaler*, Uppsala: Astronomiska Observatorium, 1973 (UGC)
- O'connell, R. W. 1976, *ApJ*, 206, 370.

- O'Neil, K. & Bothun, G. D., ApJ, 529, 811
- O'Neil, K., Bothun, G. D., & Cornell, M. E. 1997, AJ, 113, 1212 (OBC97)
- O'Neil, K., Bothun, G. D., & Schombert, J. 2000a, AJ, 119, 136
- O'Neil, K., Bothun, G. D., Schombert, J., Cornell, M. E., & Impey, C. D. 1997, AJ, 114, 2448 (OBSCI97)
- O'Neil, K., Hofner, P., & Schinnerer, E. 2000b, ApJ, 545, L99
- Osterbrock, D. E. 1989, *Astrophysics of Gaseous Nebulae and Active Galactic Nuclei* (Mill Valley: University Science Books)
- Pagel, B. E. J., Edmunds, M. G., Blackwell, D. E., Chun, M. S., & Smith, G. 1979, MNRAS, 189, 95
- Peterson, B. M. 1997, *An Introduction to Active Galactic Nuclei* (Cambridge: Cambridge University Press)
- Pierce, M. J. & Tully, R. B. 1988, ApJ, 330, 579
- Ramsey, L. W. et al. 1998, Proc. SPIE, 3352, 34
- Rönback, J. & Bergvall, N. 1995, A&A, 302, 353
- Rose, J. A. 1994, AJ, 107, 206.
- Ryder, S. D. et al. 2001, ApJ, 555, 232
- Salpeter, E. E. 1955, ApJ, 121, 161.
- Scalo, J. M. 1986, *Fundamentals of Cosmic Physics*, 11, 1
- Schombert, J. M. & Bothun, G. D. 1988, AJ, 95, 1389
- Schombert, J. M., Bothun, G. D., Schneider, S. E., & McGaugh, S. S. 1992, AJ, 103, 1107
- Schlegel, D. J., Finkbeiner, D. P., & Davis, M. 1998, ApJ, 500, 525
- Sparks, W. B. 1988, AJ, 95, 1569
- Sprayberry, D., Impey, C. D., Bothun, G. D., & Irwin, M. J. 1995, AJ, 109, 558
- Stasińska, G. & Sodr , L. 2001, A&A, 374, 919
- Storchi-Bergmann, T., Calzetti, D., & Kinney, A. L. 1994, ApJ, 429, 572
- Trager, S. C., Worthey, G., Faber, S. M., Burstein, D., & Gonzalez, J. J. 1998, ApJS, 116, 1
- Tully, R. B. & Fisher, J. R. 1977, A&A, 54, 661
- van Zee, L., Salzer, J. J., Haynes, M. P., O'Donoghue, A. A., & Balonek, T. J. 1998, AJ, 116, 2805
- van den Hoek, L. B., de Blok, W. J. G., van der Hulst, J. M., & de Jong, T. 2000, A&A, 357, 397.
- Vazdekis, A. 1999, ApJ, 513, 224 (V1999)
- Vazdekis, A. 2000, http://www.iac.es/galeria/vazdekis/MODELS_2000/out.li_BI (V2000)
- Veilleux, S. & Osterbrock, D. E. 1987, ApJS, 63, 295
- Worthey, G. 1994, ApJS, 95, 107.
- Worthey, G. 1998, PASP, 110, 888.
- Worthey, G., Faber, S. M., Gonzalez, J. J., & Burstein, D. 1994, ApJS, 94, 687
- Zabludoff, A. I. & Mulchaey, J. S. 2000, ApJ, 539, 136